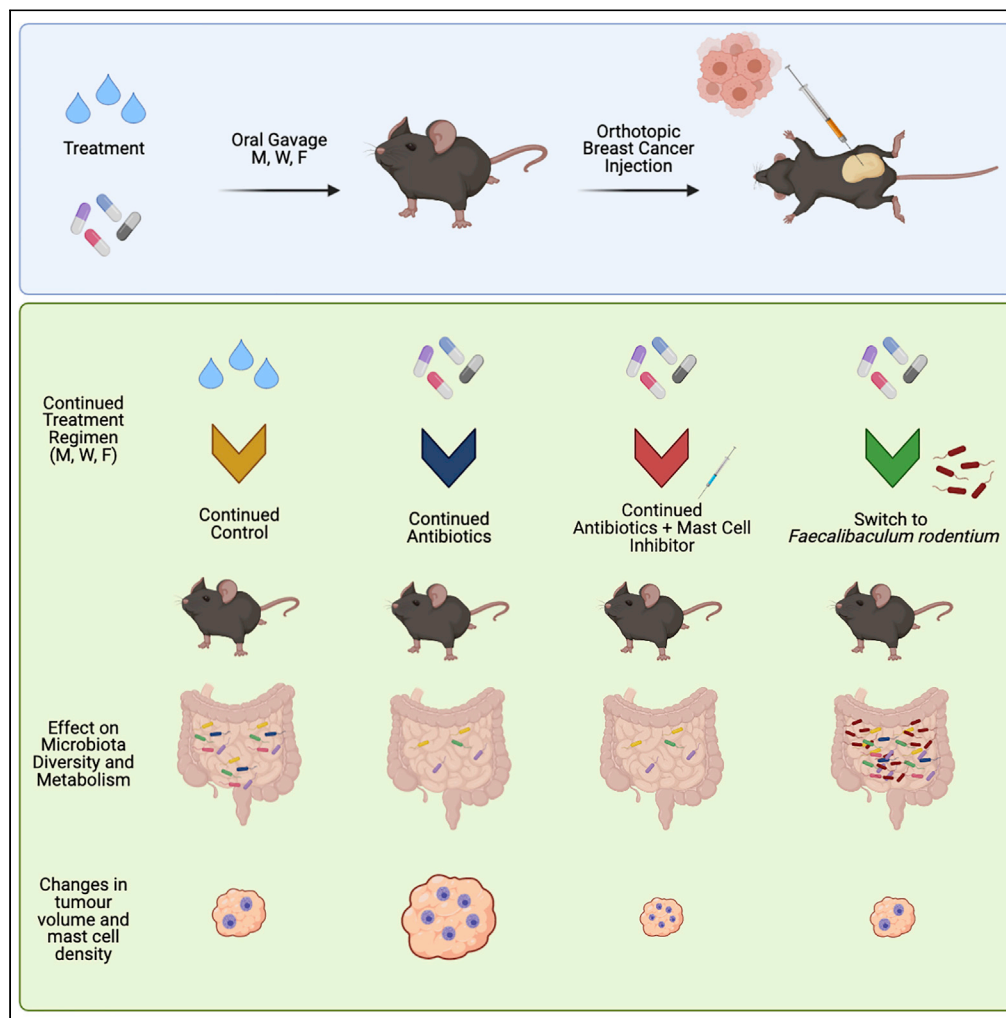CellPress
OPEN ACCESS

Article

Antibiotic-induced disturbances of the gut microbiota result in accelerated breast tumor growth

Alastair M. McKee,
Benjamin M.
Kirkup, Matthew
Madgwick, ...,
Tamás
Korcsmáros,
Lindsay J. Hall,
Stephen D.
Robinson

lindsay.hall@quadram.ac.uk
(L.J.H.)
stephen.robinson@quadram.
ac.uk (S.D.R.)

Highlights

Microbiota disturbances
promote tumor growth in
several breast cancer
models

Increased tumor volume
positively correlates with
stromal mast cell density

Supplementation with a
commensal restores
tumor growth to normal

iScience

Article

Antibiotic-induced disturbances of the gut microbiota result in accelerated breast tumor growth

Alastair M. McKee,[1,11] Benjamin M. Kirkup,[1,11] Matthew Madgwick,[1,2] Wesley J. Fowler,[1,12] Christopher A. Price,[1,12] Sally A. Dreger,[1] Rebecca Ansorge,[1] Kate A. Makin,[3] Shabhonam Caim,[1] Gwenaelle Le Gall,[3] Jack Paveley,[1,10] Charlotte Leclaire,[1] Matthew Dalby,[1] Cristina Alcon-Giner,[1] Anna Andrusaite,[4] Tzu-Yu Feng,[5] Martina Di Modica,[6] Tiziana Triulzi,[6] Elda Tagliabue,[6] Simon W.F. Milling,[4] Katherine N. Weilbaecher,[7] Melanie R. Rutkowski,[5] Tamás Korcsmáros,[1,2] Lindsay J. Hall,[1,3,8,*] and Stephen D. Robinson[1,9,13,*]

SUMMARY

The gut microbiota's function in regulating health has seen it linked to disease progression in several cancers. However, there is limited research detailing its influence in breast cancer (BrCa). This study found that antibiotic-induced perturbation of the gut microbiota significantly increases tumor progression in multiple BrCa mouse models. Metagenomics highlights the common loss of several bacterial species following antibiotic administration. One such bacteria, *Faecalibaculum rodentium*, rescued this increased tumor growth. Single-cell transcriptomics identified an increased number of cells with a stromal signature in tumors, and subsequent histology revealed an increased abundance of mast cells in the tumor stromal regions. We show that administration of a mast cell stabilizer, cromolyn, rescues increased tumor growth in antibiotic treated animals but has no influence on tumors from control cohorts. These findings highlight that BrCa-microbiota interactions are different from other cancers studied to date and suggest new research avenues for therapy development.

INTRODUCTION

As of 2020, breast cancer (BrCa) was the most frequently diagnosed cancer type globally. It was estimated to contribute 11.7% of the 19.3 million new cancer diagnoses and 6.9% of the 10 million cancer-related fatalities in 2020 (Sung et al., 2021). While ~10% of BrCa cases are linked to hereditary or somatic mutations in tumor suppressor genes, such as BRCA1 and BRCA2, the vast majority of onset cases are the result of lifestyle and environmental factors (Perez-Solis et al., 2016). Smoking, alcohol consumption, and diet have all been associated with the onset of BrCa, as well as being major contributors to disruption of gut homeostasis (Bray et al., 2018; Perez-Solis *et al.*, 2016; Teng et al., 2021; Zitvogel et al., 2017).

The gut microbiota comprises a diverse and complex array of microbes, which play an integral role in maintaining human health. Under normal healthy conditions, these microbes regulate the immune system, both locally and at sites distant from the gut (Kelly and Mulder, 2012). However, when the gut environment is altered unfavorably, following an antibiotic course for example, the microbial community profile is shifted or disturbed, and gut homeostasis is lost (Hughes et al., 2017; Zitvogel *et al.*, 2017). Alterations in the gut microbiota are associated with an array of molecular and physiological changes. Inflammatory signaling pathways can be amplified or dampened depending on changes in bacterial metabolite production, and such alterations have been associated with a variety of diseases, including cancer (Rooks and Garrett, 2016; Zitvogel et al., 2015). In colorectal cancer, a reduction in short-chain fatty acid (SCFA) production by *Roseburia* resulted in a proinflammatory cascade that promoted cancer progression in an *in vivo* mouse model (Wu et al., 2013). Additionally, a study of the gut microbiota composition of premenopausal patients with BrCa identified a reduction in the abundance of SCFA producing *Pediococcus* species compared to normal premenopausal women. The same study demonstrated the anti-cancer effects of butyrate and propionate on human BrCa cells *in vitro* (He et al., 2021). Contrastingly, inoculation of mice harboring

[1]Gut Microbes and Health Programme, Quadram Institute Bioscience, Norwich Research Park, Norwich, NR4 7AU, UK

[2]Earlham Institute, Norwich Research Park, Norwich, NR4 7UZ, UK

[3]Faculty of Medicine and Health Sciences, University of East Anglia, Norwich Research Park, Norwich, NR4 7TJ, UK

[4]Centre for Immunobiology, Institute of Infection, Immunity and Inflammation, College of Medicine, Veterinary Medicine and Life Sciences, University of Glasgow, Glasgow G12 8TA, UK

[5]Department of Microbiology, Immunology, and Cancer Biology, University of Virginia, Charlottesville, VA 22908, USA

[6]Molecular Targeting Unit, Department of Research, Fondazione IRCCS Instituto Nazionale di Tumori, Milan, 20133, Italy

[7]Department of Internal Medicine, Division of Molecular Oncology, Washington University in St Louis, St. Louis, MO, 63110, USA

[8]Chair of Intestinal Microbiome, School of Life Sciences, ZIEL – Institute for Food & Health, Technical University of Munich, 85354 Freising, Germany

[9]School of Biological Sciences, University of East Anglia, Norwich Research Park, Norwich, NR4 7TJ, UK

Continued

subcutaneous melanomas with *Bifidobacterium*, a known beneficial "probiotic" genus, has been shown to amplify the anti-tumor effect of an anti-PD-L1 immunotherapy through the priming of CD8^{+} T lymphocytes (Sivan et al., 2015). Studies like these demonstrate the microbiota's integral role in regulating local and systemic responses to cancer.

Since the discovery of penicillin in 1928, antibiotics have become an extremely effective way of preventing and fighting bacterial infections (Aminov, 2010). Nevertheless, with the evolution of antibiotic-resistant bacterial strains and an emerging understanding of the risks associated with antibiotic-induced microbiota disturbances, the frequency of their use has become increasingly controversial (Aminov, 2010; Becattini et al., 2016). The use of antibiotics in patients with BrCa is a common practice, yet their clinical benefit is under debate (Jones et al., 2014; Ranganathan et al., 2018). Additionally, the resultant alterations in the gut microbiota created by their use raise concerns over potential impacts on metabolism and inflammation that might drive tumorigenesis (Edwards et al., 2014; Tremaroli and Backhed, 2012). While the consequence of antibiotic use has been somewhat examined in other cancers, studies in BrCa are really just beginning.

A recent study by Buchta Rosean and colleagues showed that antibiotic-induced disturbances of the gut microbiota drive metastatic dissemination of an estrogen receptor-positive (ER+), luminal A mouse model of BrCa by inducing increased stromal fibrosis and intra-tumoral macrophage infiltration (Buchta Rosean et al., 2019). However, given the prevalence and heterogeneity of the disease and its variable responses to therapies, it is vitally important to understand how antibiotic-induced gut microbiota changes influence progression across the spectrum of BrCa subtypes. Using clinically relevant orthotopic mouse BrCa models of luminal B and basal-like subtypes, as well as the same luminal A model used by Buchta Rosean et al. (2019), we identified a significantly increased rate of primary tumor growth in animals subjected to broad-spectrum antibiotics. In contrast to the results described by Buchta Rosean et al. (2019), we found little variation in gross immune cell infiltration in primary tumors from animals under continuous antibiotic treatment. However, bulk and single-cell transcriptomics revealed alterations in stromal cell populations in tumors from antibiotic treated mice; we detected an increased number of mast cells in tumor stroma in these animals and demonstrated that mast cells may be drivers of the accelerated tumor progression following antibiotic-induced microbiota disturbances. Moreover, metagenomic analysis of the caecal contents of antibiotic-treated mice revealed a loss of several commensal bacterial species which correlated with elevated tumor growth. Re-supplementation of antibiotic-treated mice with one of these species, *Faecalibaculum rodentium*, restored tumor growth to control levels.

RESULTS

Treatment with broad-spectrum antibiotics results in severe perturbation of the gut microbiota and acceleration of breast tumor growth

We set out to investigate the role of the gut microbiota in regulating BrCa progression. We primarily employed an orthotopic mammary fat pad injection model using the PyMT-BO1 cell line, which exhibits a luminal B intrinsic phenotype (Su et al., 2016), representing a common (20–40%) and somewhat aggressive form of BrCa (Metzger-Filho et al., 2013).

Prior to tumor cell injection, the microbiota of animals were depleted using a cocktail of antimicrobials consisting of vancomycin, neomycin, metronidazole, amphotericin, and ampicillin (VNMAA) (Croswell et al., 2009; Reikvam et al., 2011). To maintain a continuous knockdown of the microbiota and to prevent off-target effects from bacterial regrowth, we continued antibiotic treatment throughout the experimental period. Following the regimen illustrated in Figure 1A, animals treated with VNMAA had significant microbiota knockdown after 5 days of treatment, and this knockdown persisted throughout the experimental time course (Figure 1B). Notably, these animals exhibited significantly accelerated tumor growth relative to control (water treated) counterparts (Figure 1C). When comparing treatment groups, no apparent differences in histopathology or vascular density were observed in tumors subjected to H&E and anti-endomucin immunohistochemical staining, respectively (Figures S1A and S1B). However, the number of Ki67 positive cells was increased in tumors from VNMAA-treated animals, suggesting that the antibiotic regimen promoted tumor cell proliferation (Figure 1D). Using a similar treatment regimen, we also observed enhanced tumor growth in orthotopically implanted models using EO771 cells, which more closely resemble basal-like BrCa (Ewens et al., 2005), and in BRPKp110 cells, which resemble poorly metastatic luminal A-like BrCa (Allegrezza et al., 2016) (Figure 1E), suggesting that antibiotic-induced knockdown of the microbiota drives disease progression across multiple BrCa subtypes. Using the PyMT-BO1 model, we also explored the effects of the VNMAA cocktail on metastasis. Animals were treated as described previously, with
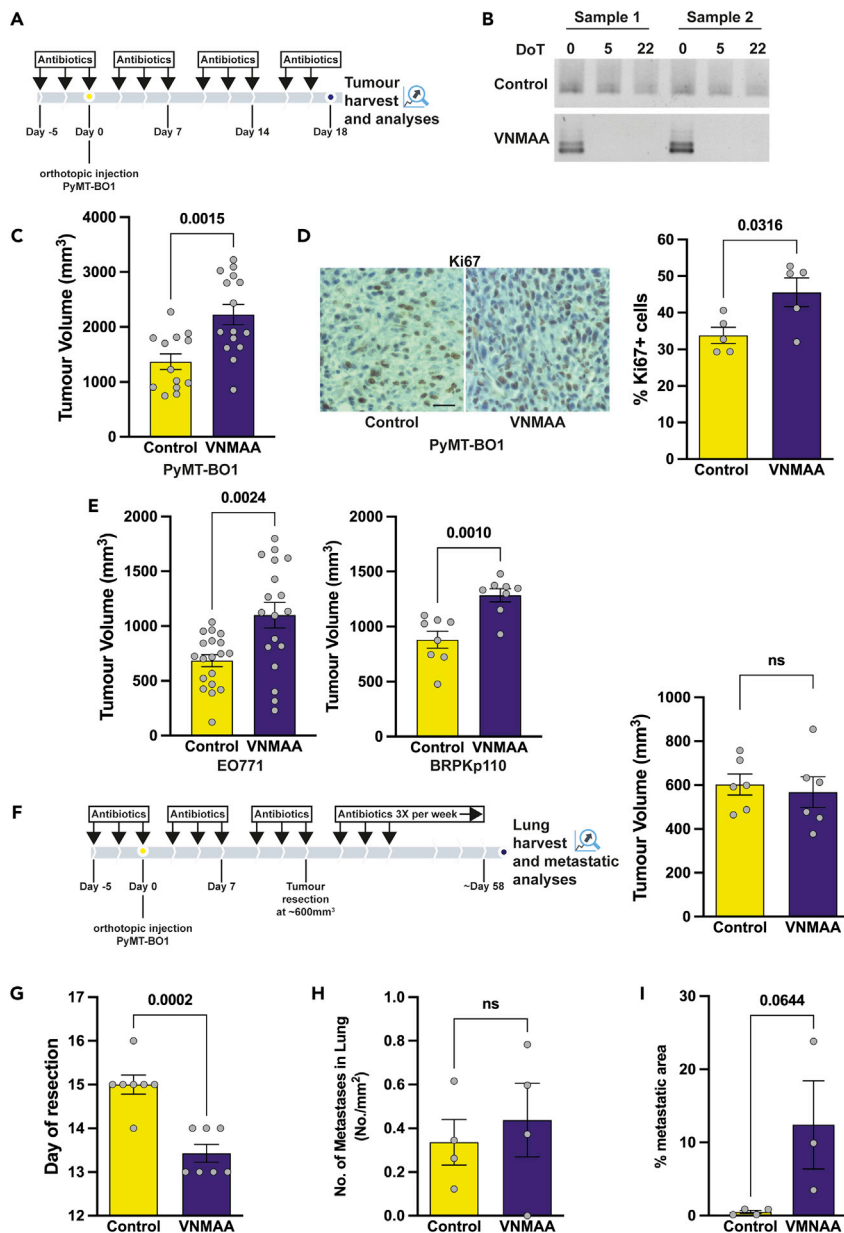
Figure 1. VNMAA-induced microbiota depletion accelerates BrCa progression

(A) Schematic of PyMT-BO1 experimental timeline; antibiotics were administered on Monday, Wednesday, and Friday for the duration of the experiment until cessation 18 days after orthotopic injection.

(B) Representative agarose gel images of 16S rRNA signatures of DNA extracted from fecal samples and amplified by PCR; DoT = days of treatment.

(C) Bar plot (mean ± s.e.m.) showing endpoint tumor volumes from VNMAA- and water-treated control animals (N = 3).

(D) Representative photomicrographs of Ki67 positive staining in PyMT-BO1 tumors following control or VNMAA treatments and the bar plot (mean ± s.e.m.) quantification of the average percentage of positive cells per frame (two frames per tumor section) (N = 1, n = 5 per condition). Scale bar represents 20 μm.

(E) EO771 and BRPKp110 tumor volumes following VNMAA treatments. The experimental setup was the same as that presented for PyMT-BO1 cells (A), but tissue harvest was performed on days 26 and 21 after orthotopic cell injection, respectively. Bar plots (mean ± s.e.m.) show endpoint volumes of the EO771 tumors (left) (N = 2) and BRPKp110 tumors (N = 1).

(F) Schematic of PyMT-BO1 metastatic studies (left), antibiotics were administered thrice weekly to experimental endpoint. The bar plot (mean ± s.e.m.) shows tumor volumes at point of resection (right) (N = 1).

(G) Bar plot (mean ± s.e.m.) showing days to tumor resection at ~600 mm³.

Figure 1. *Continued*

(H) Bar plot (mean ± s.e.m.) showing number of metastases in lungs of control and VNMAA-treated animals at experimental endpoint.

(I) Bar plot (mean ± s.e.m.) showing percent metastatic area in lungs of control and VNMAA-treated animals at experimental endpoint.

See also Figure S1.

primary tumors resected at ∼600 mm^3 (via external caliper measurements), and lungs harvested and processed ∼43 days later or at first sign of cachexia (Figure 1F). Tumors had to be resected from antibiotic-treated animals sooner (2 days on average) than from control animals due to their increased rate of growth (Figure 1G). Interestingly, the average number of metastatic lesions per animal was unchanged (Figure 1H), but the overall metastatic burden was greater in the lungs from antibiotic-treated animals due to a larger overall area occupied by lesions (Figure 1I). Thus, it is likely that while metastatic dissemination is not increased following disruption of gut homeostasis, the progression of metastatic burden is accelerated in antibiotic-treated animals similarly to primary tumor growth. Thus, we focused our attention on trying to understand what is driving the enhanced primary tumor growth that accompanies a perturbed microbiota.

VNMAA treatment severely disrupts the gut microbiota landscape

Using germ-free mice, which lack any microbiota, we sought to determine whether the increased tumor growth was the direct result of VNMAA administration or the resulting perturbation of the gut microbiota. We observed that tumor growth was not influenced by the administration of VNMAA in germ-free animals (Figure 2A). While this alludes to the importance of the microbiota in regulating tumor progression, it does not indicate if the observed elevated tumor growth observed in VNMAA-treated specific pathogen-free animals is the result of losing beneficial microbial members or the outgrowth of an antibiotic-resistant pathobiont(s).

As expected, in VNMAA-treated- mice we observed a severe knockdown of the microbiota; relative abundance of most bacterial phyla was dramatically reduced, but viruses and fungi did persist or overgrow (Figures 2B and S1C).

Concurrently, we also determined the metabolic milieu of the microbiota by performing ^{1}H NMR on caecal extracts. Unbiased principle component analysis (PCA) indicated differences in the VNMAA-treated animals when compared to control animals (Figure S1D). Further exploration of metabolites revealed that of the 96 metabolites detected, 63 were significantly different between the two groups: 21 were elevated while 42 were depleted after VNMAA treatment (Figure 2C). A number of amino acids were significantly increased in the antibiotic-treated animals, in addition to fermentation substrates such as raffinose. Conversely, SCFAs such as butyrate, acetate, and propionate and some of their conjugates (e.g. 2-methylbutryate), as well as the medium chain fatty acid caprylate, were significantly decreased after VNMAA administration. This metabolic profile further demonstrates the degree of perturbation and loss of function achieved through the VNMAA treatment as bacterial substrates (amino acids and polysaccharides) remain unprocessed in the gut while bacterial metabolites are extremely sparse.

Although we maintained antibiotic administration throughout the experimental time course and observed marked microbiota depletion in our VNMAA-treated animals, there may be still overgrowth of resistant pathobionts which act to promote disease progression, as has been previously described in other BrCa studies (Parhi et al., 2020; Rao et al., 2006). However, there is also evidence suggesting that bacterial species can improve anti-BrCa tumor immune responses (Lakritz et al., 2014). We subsequently conducted a passive fecal microbiota transfer (pFMT) experiment in which animals were exposed to fecal pellets present in bedding from the alternate treatment group. This was designed to homogenize the microbiota between experimental groups (*i.e.*, resolve microbiota drifts due to experimental treatments) (McCafferty et al., 2013; McCoy et al., 2017). As before, VNMAA treatment was started 5 days prior to PyMT-BO1 tumor cell injection. From the point of orthotopic tumor induction, bedding was swapped from animals on the alternate treatment (*i.e.* VNMAA-treated animals received bedding from the control group and vice versa). These swaps were conducted every other day until the point of tumor harvest (see schematic, Figure 2D). Exposure to VNMAA-treated feces did not increase tumor volumes in the control-treated pFMT animals suggesting that a pathobiont is not responsible for accelerated tumor growth in VNMAA-treated animals. However, regular pFMT with feces from animals with a normal microbiota led to a significant reduction in
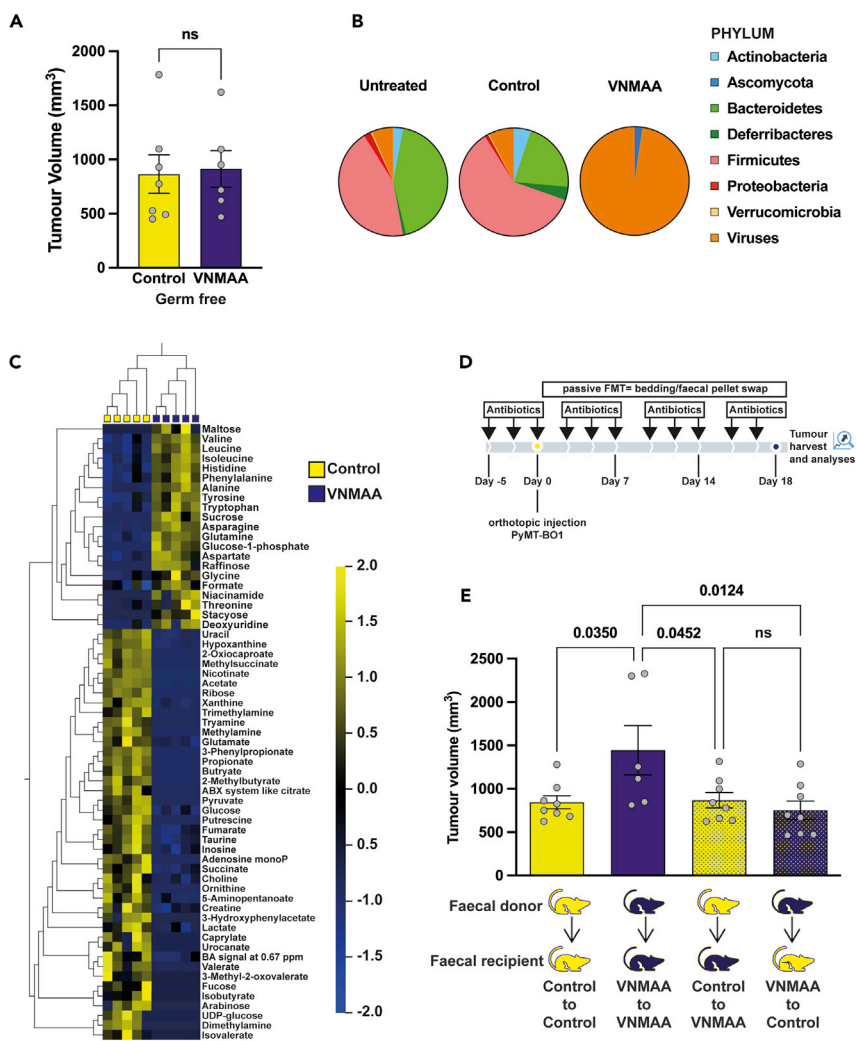
Figure 2. VNMAA administration reduces bacterial diversity and alters metabolic profiles in the gut

(A) Bar plot (mean ± s.e.m.) showing endpoint tumor volumes of PyMT-BO1 tumors grown in germ-free animals subject to VNMAA treatment (N = 1).

(B) Pie charts of shotgun metagenomics data (N = 2) showing the mean phyla-level relative abundances in caecal samples from untreated (left) (n = 3), (middle) (n = 9) control, and VNMAA- (right) (n = 6) treated animals. Untreated samples were obtained from non-tumor bearing animals.

(C) Filtered heatmap showing significantly regulated metabolites in caecal extracts of control and VNMAA-treated animals obtained through ^{1}H NMR (n = 5 individuals per condition; q < 0.01, p < 0.0025). Color ratio shown according to Log$_2$ fold change.

(D) Schematic of PyMT-BO1 passive caecal microbiota transplant (pFMT) experiment; following tumor cell injections, bedding and fecal pellets from cages not receiving bedding swaps were transferred to cages receiving the opposing treatment to donor cage. This was performed every other day to the experimental endpoint.

(E) Bar plot (mean ± s.e.m.) showing endpoint tumor volumes from pFMT experiment (N = 1).

See also Figure S1.

VNMAA-treated tumor volumes (Figure 2E), intimating that enhanced tumor progression is being driven by the loss of "protective" microbiota member(s).

Antibiotic-induced microbiota changes do not dramatically alter the tumor immune microenvironment

Prior to further profiling studies, we decided to assess tumor growth over time with PyMT-BO1 cells, given the dramatic differences observed in tumor sizes between antibiotic-treated and control animals at day 18
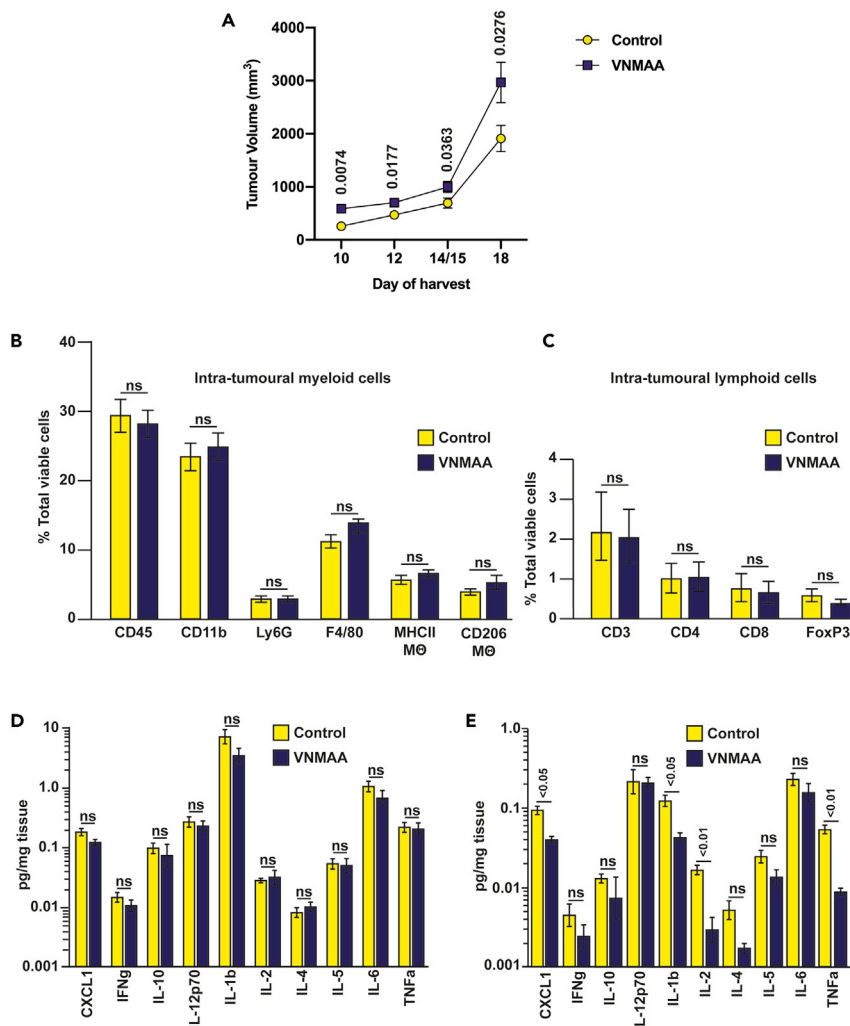
Figure 3. Immune cell populations are not altered by VNMAA administration

(A) Graph of mean ($\pm$s.e.m.) PyMT-BO1 endpoint tumor volumes at various time points: day 10 (N = 3; n $\geq$ 20 animals per condition), day 12 (N = 1; n = 14 animals per condition), day 14/15 (N = 4; n $\geq$ 19 animals per condition), and day 18 (N = 3; n = 21 animals per condition) after orthotopic injection showing growth kinetics of the model in mice undergoing either VNMAA or control treatments.

(B and C) Bar plots showing mean ($\pm$s.e.m.) percentages of (B) myeloid and (C) lymphoid tumor-infiltrating populations as determined by flow cytometry.

(D) Intra-tumoral and (E) colon-derived cytokine levels (mean $\pm$ s.e.m.) quantified by MSD V-plex assay (B–E, graphs are representative of 3 independent experiments, n = 3–5 animals per condition per experiment). MØ = macrophage. See also Figures S2 and S3.

(Figure 1C). External measurements via calipers did not indicate any difference in tumor size at onset of first palpable mass (day 7), but at each subsequent day of assessment, tumors were significantly larger in antibiotic-treated animals (not shown). However, due to the invasive nature of PyMT-BO1 tumor growth (*e.g.* extensive peritoneal adhesions which were not apparent before excision), we noted a marked difference in overall size between external caliper measurements and those taken after excision. Therefore, we performed terminal experiments at various time points in order to more accurately assess differences in primary tumor growth. At all time points examined, tumor volumes were significantly larger in animals with VNMAA-induced microbiota disturbances than those in control animals (Figure 3A). Thus, to ensure tumor size was not a major confounder in our subsequent analyses, we decided to use 15 days of tumor growth: this time point provides a balance between having sufficient material for multiple avenues of investigation with minimal differences in tumor volumes between treatment groups.
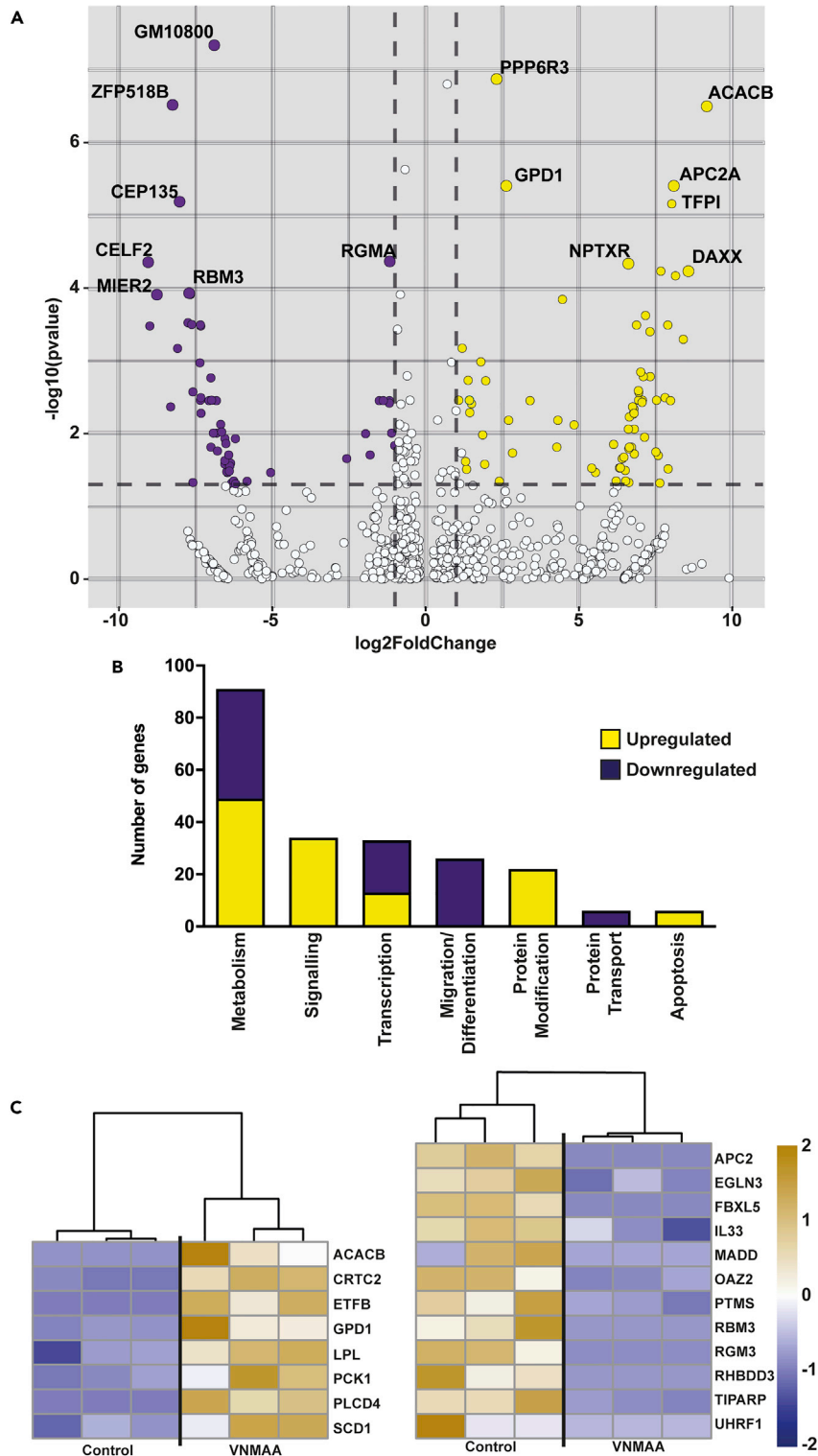
Figure 4. Intratumoral gene regulation is significantly different after VNMAA treatment, particularly in metabolic processes

(A) Volcano plot describing the parameters used for differential expression, FDR-adjusted p value < 0.05 (Log$_{10}$ adjusted) and fold change >2 (Log$_2$ adjusted). The top 7 DEGs are annotated on the graph.

Figure 4. *Continued*
(B) High-level analysis of biological process enrichment using DAVID, separated by over-arching biological function.
(C) Heatmaps showing specific genes which are related to lipid (left) and protein (right) metabolism from our DEG set. Color ratio is shown according to Log_2 fold change.

Broad-level immune cell phenotyping was performed on PyMT-BO1 tumors using flow cytometry to probe previously published links between gut microbiota-derived metabolites and the immune system (Correa-Oliveira et al., 2016). When profiling intra-tumoral CD11b$^+$ myeloid cells and proportions of F4/80$^+$ macrophages and Ly6G$^+$ granulocytes (see Figure S2A for gating strategies), we did not observe any significant changes (Figure 3B). The polarization state of tumor-associated macrophages (TAMs), using MHCII and CD206 as markers, also did not reveal any significant differences in frequency of intra-tumoral leukocytes (Figure 3B) or in the ratio of differentially polarized macrophages between treatments (Figure S2B). While the proportion of immune cells in the tumor was overwhelmingly weighted toward myeloid cells (90–95% of all CD45+ events), we also profiled T-cell populations: CD3$^+$CD4$^+$, CD3$^+$CD8$^+$, and T regulatory (T$_{reg}$) cells (CD4$^+$FoxP3$^+$). This analysis was also performed in spleen and mesenteric lymph node as a measure of peripheral immune cell populations. However, no changes were observed in the tumor (Figure 3C) or in either organ (Figures S2C and S2D). Intra-tumoral cytokine analysis also indicated no significant changes (Figure 3D). Conversely, cytokine analysis of colon tissue revealed that multiple cytokines were significantly reduced by VNMAA treatment, including CXCL-1, IL-1β, IL-2, and TNF-α (Figure 3E).

Broad-level immune cell phenotyping was also performed on EO771 and BRPKp110 tumors. Similarly to findings in PyMT-BO1 tumors, we observed no significant differences in infiltrating myeloid or lymphoid populations in these BrCa subtypes (Figure S3A).

Transcriptomic analysis of whole tumor RNA reveals a gene expression pattern consistent with changes to metabolic processes

The lack of any observed changes at a gross immunological level suggested that other more specific immune mechanisms may be contributing to the antibiotic-induced phenotype or other signaling pathways in the tumor microenvironment might be driving accelerated tumor growth in VNMAA-treated animals. To address these questions, we undertook global transcriptomic sequencing and analysis of whole tumors which yielded a total of 172 differentially expressed genes (DEGs): 85 upregulated and 87 downregulated in the tumors from VNMAA-treated animals (Figure 4A). To our suprise, functional clustering (using NIH DAVID) indicated no differential regulation of immune-related pathways. However, a high frequency of processes involved in cellular metabolism was identified. In total, 91 of 172 DEGs were associated with metabolic transduction, transcription, migration, and differentiation (Figure 4B). More detailed GO definitions indicated significant changes in lipid metabolism, gluconeogenesis, and protein metabolism. Further analysis of these biological functions revealed two major groups of genes: genes such as ACACB, LPL, and ACSL1, belonging to lipid metabolism, were upregulated in samples from VNMAA-treated mice; several other genes, such as FBXL5, MADD, OAZ2, and TIPARP, relating to protein modification or metabolism, were downregulated in samples from VNMAA-treated animals (Figure 4C).

Single-cell RNAseq of tumors from VNMAA-treated animals reveals changes in stromal cell populations

Although antibiotic-induced changes in the gut microbiota may drive changes in metabolic pathways used by PyMT-BO1 tumors to accelerate primary growth, we conjectured these differences were likely consequential of alterations in tumor progression, rather than direct drivers. The lack of any observed alteration in the "classical" tumor immune microenvironment in VNMAA-treated animals, particularly given the known association between TAMs and PyMT mouse models (Qian and Pollard, 2010), and the study from Buchta Rosean et al. demonstrating antibiotic-induced alterations in macrophage recruitment to luminal A mouse models of BrCa (Buchta Rosean et al., 2019) suggested either functional differences within populations and/or changes in other atypical or rare immune populations in tumors from VNMAA-treated mice. To capture possible differences in cell-type behavior between treatments, we profiled the tumor microenvironment at single cell (sc) resolution using day 13 samples to test for early potential immune-mediated changes. Uniform Manifold Approximation and Projection (UMAP) analysis (Becht et al., 2018) revealed 21 clusters, representing both tumor cells and cells of the tumor microenvironment (Figure 5A). Some of these clusters represented tumor infiltrating immune cells including macrophages, B cells, and T cells.
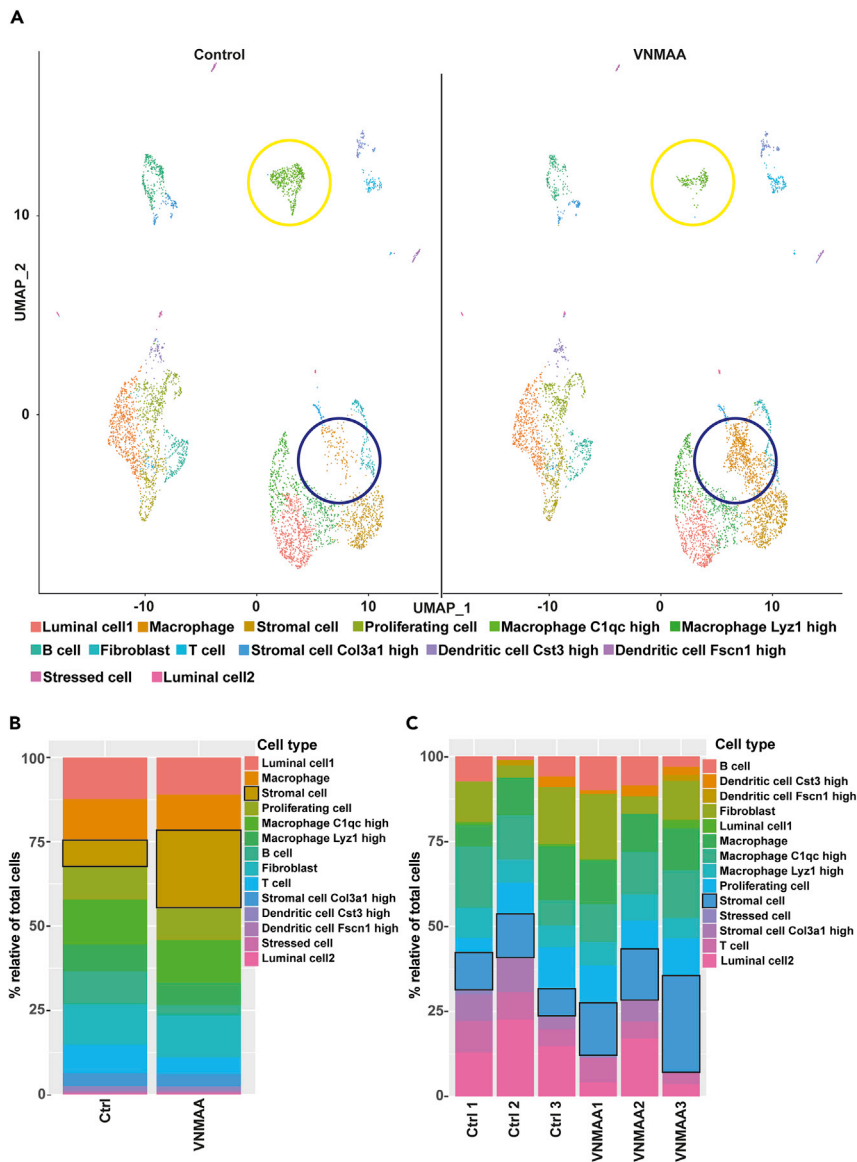
Figure 5. VNMAA treatment alters cellular profile of the tumor microenvironment

(A) UMAP clustering of cell types identified through single-cell RNAseq of tumors from control (left) and VNMAA (right)-treated animals. Pooled data from 2 animals per condition. Yellow circles denote B-cell populations; purple circles denote a stromal cell cluster.

(B) Percent abundance of cell types relative to the total number of cells per treatment group sequenced through single-cell RNAseq (pooled data from 2 samples per treatment).

(C) Percent abundance of cell types relative to the total number of cells per sample following deconvolution of bulk RNAseq presented in Figure 4 (n = 3 samples per condition). See also Figure S4.

While the overall number of cells in most identified clusters was broadly similar between each treatment, UMAP clustering revealed two clear differences in tumors from VNMAA-treated animals compared to controls: reduced B-cell numbers and increased cells within one of two stromal populations (Figures 5A and 5B). B cells can play anti-tumorigenic roles in some settings (Carmi et al., 2015; DiLillo et al., 2010; Tao et al., 2015). However, after applying the same gene signatures used to define clusters in the scRNAseq to our deconvoluted bulk RNAseq data on day 15, we observed no obvious differences in percentages of B-cell signatures between conditions (Figure 5C). This further correlated with additional flow cytometric analyses, showing no differences between control and VNMAA-treated tumors with respect to B-cell numbers at day 15 (Figure S3B). In support of these findings, this immune population is not generally
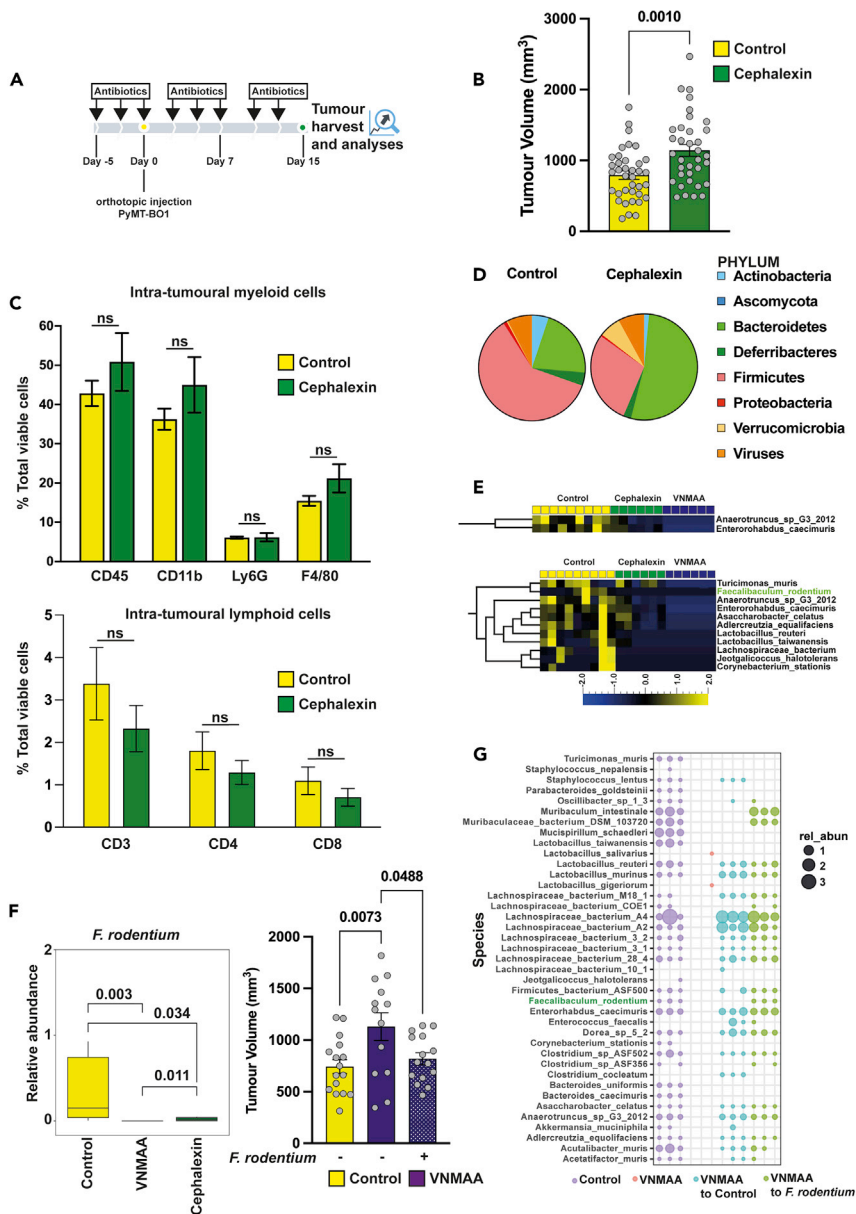
Figure 6. Clinically relevant antibiotic, cephalexin, accelerates tumor growth

(A) Schematic of PyMT-BO1 experimental timeline; cephalexin was administered on Monday, Wednesday, and Friday for the duration of the experiment until cessation 15 days after orthotopic injection.

(B) Bar plot of mean (±s.e.m.) endpoint tumor volumes from cephalexin-treated versus water-treated animals (N = 3).

(C) Bar plots show mean (±s.e.m.) percentages of viable cells of myeloid (top) and lymphoid (bottom) tumor-infiltrating populations as determined by flow cytometry (representative of 3 independent experiments).

(D) Pie charts of shotgun metagenomics data (N = 2) showing the mean phyla-level relative abundances in caecal samples from control (left) (n = 9) and cephalexin (right) (n = 6)-treated animals.

(E) Filtered heatmap showing hierarchal clustering of bacterial species with significantly different relative abundances following a two-group comparison of both antibiotic treatments versus control samples (p = 0.001, q < 0.05) (top); and a filtered heatmap showing hierarchal clustering of bacterial species relative abundances following a two-group comparison of both antibiotic treatments versus control samples with relaxed statistical parameters (p < 0.05, q = 2.085) (bottom); relative abundances were determined by shotgun metagenomics of caecal contents (n ≥ 6 individuals per condition); color ratio shown according to Log₂ fold change.

(F) Box and whisker plot (left) showing significantly reduced relative abundances of *Faecalibaculum rodentium* (*F. rodentium*) in both VNMAA and cephalexin-treated samples (N = 2) and a bar graph (right) of PyMT-BO1 tumor volumes at experimental endpoint (day 15). Experimental setup as in (A). Control animals (yellow bar) were gavaged three

Figure 6. *Continued*
times per week (Monday, Wednesday, Friday) to point of tissue harvest. VNMAA animals were gavaged with antibiotics (every Monday, Wednesday, Friday) to the point of a palpable tumor (day 7 post orthotopic injection), at which point they were switched to either water (purple bar) or to *F. rodentium* (purple stippled bar).
(G) Bubble plot showing metagenomic changes in relative abundance of several bacterial species in caecal samples at experimental endpoint following treatment regimens as described. See also Figures S5 and S6.

considered a major player in the MMTV-PyMT tumor model (DeNardo et al., 2009). We, therefore, decided to focus our attention on the stromal cell cluster. Both scRNAseq (Figures 5A and 5B) and deconvoluted bulk RNAseq (Figure 5C) suggested this stromal cluster was increased in cell numbers in tumors from VNMAA-treated mice. Closer examination of the gene signature of this cluster identified a number of collagen transcripts (Figure S4A). Given the known links between collagen, fibrosis, and BrCa progression (Boyd et al., 2007; Huo et al., 2018) and recent work showing fibrosis is increased in response to antibiotic-induced microbiota perturbations in the luminal A model (Buchta Rosean et al., 2019), we hypothesized that this may also be the case in our luminal B model. However, Picro-Sirius Red staining (which demarcates collagen fibers) of tumor sections from control and VNMAA-treated animals did not show any obvious differences in stromal collagen deposition when comparing the two conditions (Figure S4B).

Clinically relevant antibiotics induce similar phenotypic changes in primary tumor growth and tumor immune cell infiltration

VNMAA treatment allowed us to establish a link between microbiota homeostasis and tumor growth kinetics, but the induced disturbances are severe, with loss of many bacterial species (Figure 2A) and large shifts in gut metabolite profiles (Figure 2B). We therefore investigated the effects of a more clinically relevant antibiotic in our PyMT-BO1 model. After discussing prevalent antibiotic usage with our clinical colleagues (US and UK), we decided to perturb the microbiota with cephalexin, a broad-spectrum beta-lactam antibiotic that targets gram-positive bacteria (Bush and Bradford, 2016). Using an administration protocol identical to that of VNMAA (Figure 6A), mice were gavaged with patient-relevant doses of cephalexin (35 mg/kg in humans) (thrice weekly), starting 5 days prior to orthotopic injection of PyMT-BO1 cells until tumor harvest (day 15). Primary tumor growth was significantly accelerated in cephalexin-treated animals (Figure 6B). A similar change in tumor growth kinetics led us to compare the two different antibiotic treatments relative to control cohorts, and as observed in VNMAA-treated animals, we saw no gross changes in tumor infiltrating myeloid or lymphoid cell populations by flow cytometry (Figure 6C).

As expected, the microbiota changes induced by cephalexin were much less drastic than those resulting from VNMAA administration with only a few taxa increasing and decreasing relative to control (Figures 6D and S1C). Given we hypothesize accelerated tumor growth is driven by the loss of tumor protective microbiota members, we analyzed caecal samples from control, VNMAA, and cephalexin-treated animals using whole genome shotgun sequencing to understand the effect on bacterial abundances at a species level. Given the VNMAA cocktail ablated the bacterial element of the microbiota almost entirely, alongside our hypotheses of a loss of an anti-tumorigenic microbiota member(s), we performed unsupervised clustering via a two-group comparison (control versus both antibiotic-treated samples), with a false discovery rate (FDR) correction set to $q < 0.05$, to identify species which were reduced similarly in both antibiotic groups. This analysis suggested the common loss of only 2 of 52 assigned bacterial species (*Enterorhabdus caecimuris* and *Anaerotruncus* sp. G3_2012) between the two different antibiotic regimens, neither of which have been particularly associated with cancer (Figure 6E top). However, when relaxing the FDR parameters and filtering for species with an uncorrected p value of $p < 0.05$, we identified 11 which were reduced in both cephalexin and VNMAA samples relative to control (Figure 6E bottom). Of these, several have already been associated with immune regulatory and anti-tumorigenic roles. Of immediate interest was the reduction of *Faecalibaculum rodentium*, which was recently observed to have a protective role in an Apc[Min/+] spontaneous mouse model of colorectal cancer, as well as in wild-type C57BL/6 mice induced with colorectal cancer through administration of azoxymethane and dextran sulfate sodium (Zagato et al., 2020). A targeted Wilcoxon test of *F. rodentium* abundances in cephalexin and VNMAA compared to control samples confirmed it was significantly reduced in both VNMAA- and cephalexin-treated samples (Figure 6F, left). Subsequently, we tested whether supplementation with *F. rodentium* would rescue the enhanced tumor growth induced by antibiotics. Using the previously described antibiotic treatment regimens (see schematics Figures 1A and 6A), animals were treated with vehicle (control) or VNMAA thrice weekly to point of a palpable tumor; at this point, control animals continued to receive vehicle only, while

half of the VNMAA animals were shifted to vehicle treatment (VNMAA to control), and the other half were treated with *F. rodentium* (VNMAA to *F. rodentium*). These treatments continued thrice weekly to the point of tissue harvest (day 15). VNMAA to control animals showed accelerated tumor growth, but we observed reduced tumor growth in VNMAA to *F. rodentium* treated animals (Figure 6F, right), suggesting this species may contribute to a protective role of the microbiota in regulating BrCa. Shotgun metagenomics of caecal contents confirmed the loss of *F. rodentium* in VNMAA to control animals and its return in VNMAA to *F. rodentium* animals (Figure 6G).

Previous metabolic analysis of VNMAA caecal samples compared to controls had shown a significant inhibition of gut function based on the inverse abundances of high levels of bacterial substrates but reduced metabolites. However, as metagenomic analysis highlighted a markedly reduced alteration in bacterial diversity following cephalexin treatment compared to VNMAA, we sought to identify whether there was any obvious change in metabolite abundance which may be associated with tumorigenic influence in the breast. While there was some variability between the samples from cephalexin-treated animals, the profiles generally had more in common with samples from the control cohort than they did with the VNMAA group. However, similarly to VNMAA samples, several amnio acids (leucine, isoleucine, valine, and tryptophan) were increased. To our surprise, there were far fewer similar comparisons for bacterial-derived metabolites, such as the SCFAs butyrate, acetate, and propionate, though levels of the medium chain fatty acid caprylate were generally repressed (Figure S5). However, multiple t-tests with a corrected Q statistic identified only adenosine monophosphate as being significantly reduced in cephalexin samples versus control (p = 0.000447, q = 0.05). In an attempt to link the cephalexin-induced changes in gut taxonomic profiles and metabolism with the observed increase in tumor growth, a functional analysis using confint() from the coin package was performed on the shotgun metagenomics data to identify possible bacterial pathways which may be linked to disease progression. However, of the 93 pathways which were identified, only six were significantly different in their "abundance" relative to controls. Three were increased while the other three were decreased in their activity in samples from cephalexin-treated animals (Figure S6). Of those pathways identified as significantly changed, only the *Bifidobacterium* shunt, depressed in cephalexin-treated animals, suggested any potential link to SCFA production. Despite this, SCFA metabolites (e.g. acetate and propionate) were not significantly altered in this group of animals.

Antibiotic-induced stromal mast cells accelerate tumor growth

Given the accelerated tumor growth that occurs in both VNMAA- and cephalexin-treated animals, it is intriguing to speculate a common driver associated with these responses. Although our previous analyses did not indicate any obvious "candidates", including immune populations, closer examination of the transcript profile of the stromal cell cluster (from our scRNAseq analysis) indicated the presence of a number of transcripts expressed by mast cells (*e.g.* Mcpt1, Mcpt8, and Cma1). Moreover, while we did not observe any gross differences in tumor fibrosis when comparing tumors from control and VNMAA-treated mice, examination of Picro-Sirius Red-stained tumor sections from VNMAA-treated samples at higher magnification indicated a number of granular cells predominantly situated in tumoural stroma which were reminiscent of mast cells. Toluidine Blue staining of tumor sections confirmed their identity as mast cells (Figure 7A). Importantly, quantitation of mast cells showed increased stomal numbers in sections from VNMAA-treated mice, particularly in the extra-tumoral stroma (Figure 7B). Moreover, while we did not observe statistically significant changes in mast cell numbers in tumors harvested from our *F. rodentium* studies, there were generally reduced numbers of mast cells in VNMAA to *F. rodentium* treated animals compared to VNMAA to control animals (Figure 7C). Given our speculation of a common mechanism driving accelerated primary tumor growth following antibiotic-induced microbiota perturbations, we also enumerated mast cell numbers in EO771 tumors from VNMAA-treated animals and in PyMT-BO1 tumors from cephalexin-treated animals; both showed significantly increased mast cell numbers in the tumor stroma of antibiotic-treated mice compared to controls (Figures 7D and 7E, respectively). We observed similar findings in the BRPKp110 luminal A tumor model from animals treated with vancomycin, neomycin, metronidazole, gentamicin, and ampicillin (VNMGA) (Figure 7F) and in a Her2-neu spontaneous model in animals treated with vancomycin only (Figure 7G).

Collectively, these observations prompted us to question whether this, previously overlooked, population of myeloid-derived immune cells was responsible for accelerated primary tumor growth in antibiotic-treated animals. In an attempt to determine whether targeting mast cell function influences tumor growth, we treated both control and VNMAA-treated mice with cromolyn, a mast cell stabilizer which prevents
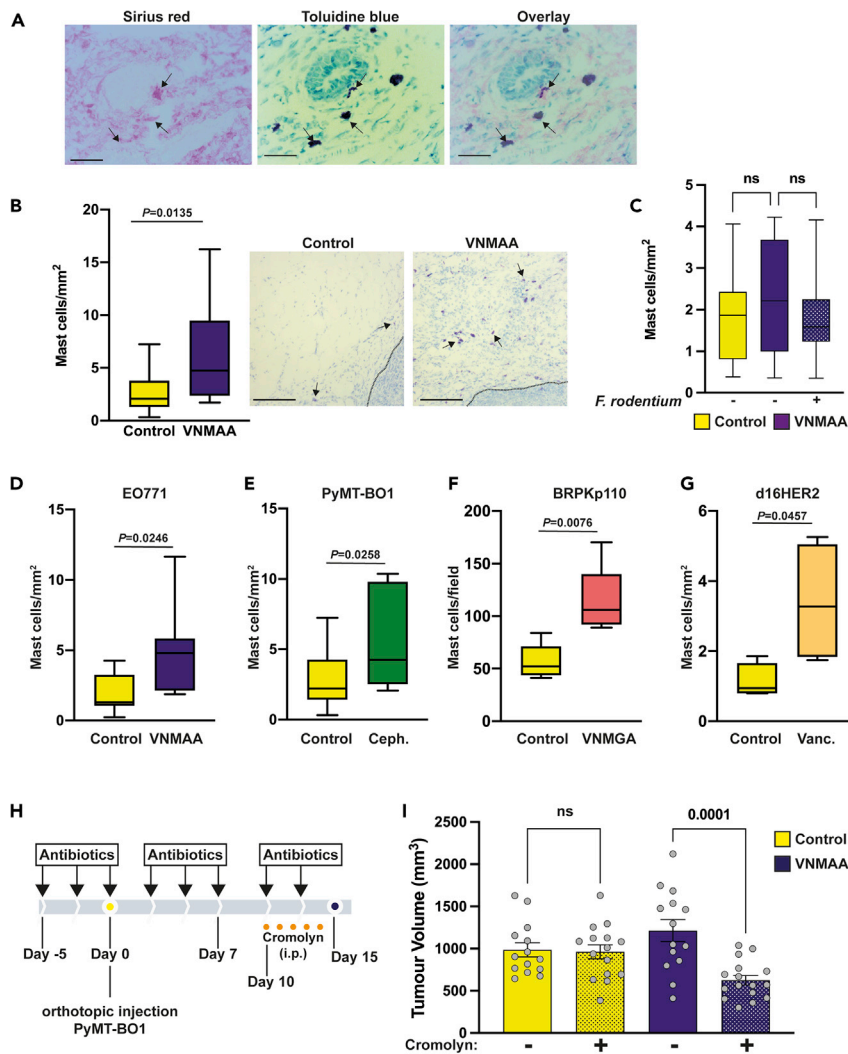
Figure 7. Increase in stroma associated mast cells promotes tumor growth following VNMAA treatment

(A) Histological staining for collagen deposition (Picro-Sirius Red), mast cells (toluidine blue), and their co-localization (overlay) in a representative image of a tumor from a VNMAA-treated animal. Arrows point to mast cells. Scale bar represents 100 μm.

(B) Bar and whisker plot of mast cell density (mast cells/mm^2) in PyMT-BO1 tumors from control and VNMAA-treated animals (left) and toluidine blue-stained MCs present in peripheral tumor stroma (dotted line denotes tumor margin; arrows point to mast cells; scale bar reprsents 50 μm. N = 2; n ≥ 13 animals per condition).

(C) Mast cell counts in *F. rodentium* study.

(D) Bar and whisker plot of mast cell density in EO771 tumors from control and VNMAA-treated animals (N = 2; n ≥ 7 animals per condition).

(E) Bar and whisker plot of mast cell density in PyMT-BO1 tumors from control and cephalexin-treated animals (N = 1; n ≥ 5 animals per condition).

(F) Bar and whisker plot of mast cell density in BRPKp110 tumors from control and VNMGA-treated animals (N = 1; n = 5 animals per condition).

(G) Bar and whisker plot of mast cell density in d16HER2 tumors from control and vancomycin-treated animals (N = 1; n = 4 animals per condition).

(H) Schematic of experimental timeline for mast cell inhibition experiment using cromolyn administered over the last 5 days of the experiment.

(I) Bar plot of mean (±s.e.m.) endpoint tumor volumes of cromolyn-treated animals with either water or VNMAA versus control counterparts (N = 2); images below are photographs of representative whole tumors from each condition. Scale bar represents 5mm.

degranulation (Zhang et al., 2016) (see Figure 7H for experimental regimen). During the final 5 days of tumor growth, mice were treated with either cromolyn (10 mg/kg, delivered i.p.) or normal saline as a vehicle control. As expected, tumors were significantly larger in VNMAA-treated animals when compared to control animals. Notably, cromolyn inhibited tumor growth in antibiotic treated animals but had no influence on control animals (Figure 7I). These data suggest a potential role for mast cells in BrCa progression in animals with an antibiotic-induced disturbed microbiota.

DISCUSSION

The use of antibiotics is widespread among patients with cancer to prevent opportunistic infection, both prophylactically prior to surgery and during periods of immune compromisation. However, the rising threat of antibiotic-resistant pathogens highlights the importance of re-evaluating antibiotic use in the clinic. Antibiotic-resistant infections kill hundreds of thousands of people per year worldwide, and this figure is expected to grow exponentially over the next 30 years (Mullard, 2016). Moreover, some evidence suggests that antibiotic use may not be beneficial to all patients. Recent studies have demonstrated an unequivocal role of the patient microbiome in orchestrating anti-tumor responses, and many have found that the use of antibiotics compromises treatment efficacy in several cancers (Velicer et al., 2004, 2006). It is therefore prudent that clinicians begin to carefully consider the efficacy of antibiotic use in their patients. To do so, we must fully understand how the microbiota impact different cancer pathologies. Other groups have made progress in understanding how antibiotics affect immunogenic cancers (Gopalakrishnan et al., 2018; Matson et al., 2018; Routy et al., 2018; Vetizou et al., 2015); however, to date, only a small number of studies have looked at their effects on BrCa (Buchta Rosean et al., 2019; Rossini et al., 2006; Teng et al., 2021).

Using clinically relevant BrCa models, we set out to understand whether the use of antibiotics has any impact on tumor progression. In luminal B (PyMT-BO1), basal-like (EO771), and luminal A (BRPKp110) BrCa tumor models, a prolonged disruption of the gut microbiota via antibiotic treatment resulted in accelerated tumor growth. This suggests that antibiotic treatment is detrimental across multiple BrCa intrinsic subtypes. In addition to those described in this paper, Buchta Rosean et al. (2019) employed antibiotic treatment which incorporated a 4-day recolonization period following a two-week antibiotic administration prior to tumor induction and observed increased metastasis to the lungs in the BRPKp110 luminal A BrCa model. Together, these results support the hypothesis that antibiotics negatively impact the microbiota which in turn negatively impacts the disease outcome of BrCa.

Use of antibiotics has been shown to impact tumor growth in both pre-clinical and human studies. However, these studies largely focus on the influence of the microbiota on anti-tumor therapies. For example, Vetizou et al. and Routy *et al.* probed the impact of antibiotics on anti-CTLA4 and anti-PD-1 therapies, respectively, finding that these treatments are rendered ineffective when the microbiota is depleted (Routy et al., 2018; Vetizou et al., 2015). However, when comparing control and antibiotic-treated animals without administration of anti-tumor agents, these groups found no difference in tumor volume. This suggests that our findings may be specific to BrCa subtypes and are supported by Rossini et al., who in 2006 demonstrated, using HER2/*neu* transgenic mice, that antibiotic administration alone increased the incidence of spontaneous BrCa (Rossini *et al.*, 2006).

Importantly, we show that an antibiotic that is used widely in patients with BrCa (cephalexin) accelerates the progression of BrCa in the PyMT-BO1 model. This is a particularly intriguing observation as it suggests that even relatively small deviations from microbiota homeostasis can negatively impact BrCa progression. To date, there have been no human studies linking microbiota disruptions causatively to BrCa progression. However, several human studies have described a loss of gut microbial diversity in patients with BrCa compared to normal control subjects (Goedert et al., 2015; Guan et al., 2020; Wu et al., 2020; Zhu et al., 2018). Thus, our observations intimate that, in these studies, the microbiota may be influencing BrCa progression rather than changing as a consequence of it.

Given the results of our passive FMT study (Figure 2E), we hypothesize that a loss of mutualistic microbiota members is responsible for the accelerated progression (rather than the amplification of a pathobiont). A direct comparison of the microbiota profiles between VNMAA-treated and cephalexin-treated animals (compared to controls) showed reduced relative abundance of *Lactobacillus reuteri*, *Lachnospiraceae bacterium*, and *F. rodentium*, among others. Many of these species are postulated to play anti-tumorigenic roles in a number of different cancers (Rasouli et al., 2017; Viaud et al., 2013; Zagato et al., 2020).

F. rodentium was particularly interesting to us, given its recently proven role in limiting the development of colorectal cancer in mouse models (Zagato et al., 2020). Based on the evidence from the pFMT study suggesting the driver for tumor progression was likely the loss of commensal bacterial species, we supplemented antibiotic-treated animals with *F. rodentium* and observed a significant reduction in tumor volumes versus "control supplemented" animals. However, several "probiotic" studies have described improved efficacy when using a cocktail of microbes, often from several genera. For example, Tanoue et al. (Tanoue et al., 2019) demonstrated that administration of an 11-strain commensal cocktail, isolated from human fecal samples and associated with improved CD8 T cell activity, to germ-free mice with engrafted MC38 adenocarcinoma tumors resulted in improved anti-tumor responses during anti-PD-1 checkpoint inhibitor therapy. Additionally, the commercial probiotic VSL#3, which comprises a combination of *Bifidobacteria*, *Lactobacillus*, and *Streptococcus* species, has been shown to prevent colitis-associated colorectal cancer in rats (Appleyard et al., 2011). We have yet to test the other commonly reduced species in this way, but it is possible that a cocktail of these commensals may improve anti-tumor rescue effects further. Noteworthy, however, is the observation that some of the identified potentially beneficial species supressed by VNMAA treatment (*L. reuteri* and many of the *L. bacterium species*, for example) return after antibiotic treatment is halted (e.g. in VNMAA to control animals – Figure 6G). Without the addition of *F. rodentium*, the repopulation of the microbiota by these species does not appear to reduce tumor growth, at least within the timescale of the experiments. This suggests that either *F. rodentium* is playing a key anti-tumorigenic role or its presence within a complex "cocktail" of beneficial commensals is important; we cannot currently rule out either possibility.

While NMR analysis clearly demonstrated a dramatic loss of microbial-derived metabolites (e.g. SCFAs), in the VNMAA-treated animals, there were far fewer differences in the cephalexin samples, which correlates with the more subtle microbial taxa changes using a single vs. a cocktail antibiotic regimen. Of those metabolites profiled in cephalexin-treated animals, it is unlikely that any of these are solely responsible for driving increased tumor growth. In the absence of clear metabolic differences as well as any gross changes in canonical pro- or anti-tumorigenic immune populations in our models, we decided to employ RNA sequencing of whole tumor extracts to gain further mechanistic insight and/or perhaps uncover alterations in immune activation pathways (as opposed to overall cell numbers) that might explain accelerated tumor progression in antibiotic-treated mice. Here too, however, we did not detect any differences in immune signatures between control and antibiotic-treated animals. Rather, biological process enrichment analysis showed that alterations were predominantly seen in metabolic processes, particularly in lipid and protein metabolism. Metabolic reprogramming is a well-established hallmark of cancer, and upregulation of lipid metabolism is strongly associated with tumorigenesis, particularly in BrCa (Benito et al., 2017; Naeini et al., 2019; Zhang et al., 2019). In addition to changes in lipid metabolism, several genes associated with protein metabolism were downregulated by VNMAA treatment, and many of these genes are known tumor suppressors. While these findings provide therapeutic avenues to explore for combating the deleterious effects of antibiotic use, we felt they were more likely a readout of accelerated disease progression, rather than a direct consequence of microbiota perturbation.

As mentioned above, Buchta Rosean et al. (2019) demonstrated striking findings using the BRPKp110 luminal A model with a similar antibiotic cocktail. They observed that microbiota disruption resulted in enhanced metastatic dissemination as well as the establishment of a tumor microenvironment that favors elevated macrophage infiltration and increased tumor fibrosis. Therefore, we decided to probe immune signatures in more detail, via in-depth scRNAseq analyses of control and VNMAA-treated tumors. Although we observed a reduction in B-cell profiles in antibiotic treated tumors (Figure 6), flow cytometry studies (at a later time point) and deconvolution of the bulk RNA-sequencing data did not reveal any differences in this immune population. Therefore, although it may be speculated that in the PyMT-BO1 BrCa model B cells play an (early) anti-tumorigenic role, further studies are required to probe this in more detail. Notably, previous studies have indicated B cells can both promote and inhibit cancer progression (Yuen et al., 2016), and mice specifically lacking B cells were unaffected in terms of tumor latency or progression in the MMTV-PyMT model (DeNardo et al., 2009), highlighting the complexity and dynamic nature of specific immune cell populations in cancer models.

A further immune-linked signature that was observed with scRNAseq was an increased stromal profile in tumors from VNMAA-treated mice. This initial finding and subsequent histological analysis revealed an increase in a discreet immune cell population in tumors from antibiotic-treated mice; antibiotic-induced

microbiota perturbations increased mast cell numbers in tumor stroma and when functionally blocked (i.e. blocking granule release), tumor growth was reduced, highlighting that this cell type is likely a key driver of accelerated tumor growth after antibiotic-induced microbiota perturbations (Figure 7). As with most immune cells, mast cells have been shown to play both anti- and pro-tumourigenic roles in multiple cancers (Varricchi et al., 2017) including BrCa (Aponte-Lopez et al., 2018). He et al. showed that when mast cell-deficient mice (Kit[W-sh/W-sh]) are crossed with MMTV-PyMT mice, tumor growth and metastatic potential are significantly curtailed (He et al., 2016). Importantly, the data presented suggest that microbiota disturbances increase mast cell homing to tumors and/or their increased proliferation within tumors. This correlation holds true in every subtype of BrCa we have so far examined, suggesting a universal mechanism driving the response. However, as mast cell inhibition of control animals had little impact on tumor progression, it is likely there is differential regulation of their pro-tumorigenic function specifically by the microbiota. There is precedent in the literature to suggest an interplay between the gut microbiota and mast cell function: germ-free mice exhibit mast cells with impaired functionality (Schwarzer et al., 2019), and multiple interactions between mast cells and microbiota members are known to regulate mast cell activation (De Zuani et al., 2018), though these studies are largely restricted to mucosal mast cells. Intriguingly, both SCFAs and amino acids are capable of regulating mast cell function (Lechowski et al., 2013; Wang et al., 2018).

In conclusion, our work has shown that disruption of the gut microbiota via antibiotics has detrimental impacts on BrCa progression. We speculate that antibiotic-induced loss of a beneficial microbiota specie(s) has the potential to release the "brakes" on tumor growth by re-programming mast cell homing and/or function. Our future studies will focus on understanding from "where" increased mast cells are coming, "what" changes are occurring in mast cells in response to microbiota disruption, "who" is responsible for inducing these changes, and "how" they promote them.

Limitations of study

As with most murine studies of the gut microbiota, there are some important limitations to note. Firstly, we have employed broad-spectrum and systemically administered antibiotics, so we cannot entirely rule out that microbiotas beyond the gut are contributing to observed phenotypes. However, we do feel this concept is somewhat mitigated against by the *F. rodentium* studies in which microbiota supplementation was applied directly to the gut; these studies demonstrate a return to normal tumor growth after *F. rodentium* supplementation.

Secondly, due to the targeted nature of ^{1}H NMR, it is possible that metabolites which were not included in these analyses may be differentially abundant between treatment groups, particularly when comparing samples from control versus cephalexin-treated animals. This may explain why no obvious links between the pathways identified in the shotgun WGS dataset were linked with associated changes in metabolite concentrations in caecal samples from cephalexin-treated animals. Interestingly, *F. rodentium* has been linked to butyrate production, but butyrate levels did not change in response to cephalexin treatment.

Thirdly, while shotgun WGS approaches have significantly improved the depth at which the microbiota composition can be described, there are still several areas where descriptive data are lacking. For example, proportionally there are far more annotated genomes for bacterial organisms than there are for fungi and viruses. Our data had many "unassigned" reads which are likely linked to undescribed organisms. It is possible that these organisms may play a role in a perturbed microbiota which influences our BrCa models.

Fourthly, for our scRNAseq analyses, we employed 10X Genomics technology, which uses a short read platform to identify cell types. While this was ideal for obtaining a broad overview of the cell types within the tumor microenvironment, it likely curtailed our ability to detect differences in small populations of cells (e.g. mast cells) or in specific biological processes. A longer read platform would improve both aspects.

Finally, our study employed the use of cromolyn sodium as a drug to inhibit mast cell function. However, cromolyn does not specifically target mast cells alone. It has been associated with inhibitory effects on other granulocytes, such as basophils (Mazurek et al., 1980). There is also some debate in the literature as to whether cromolyn is effective at inhibiting mast cell degranulation in mice (Oka et al., 2012) and as to whether it can elicit its effects over a short time course (Minutello and Gupta, 2021). As such, in order to improve the translational relevance of these studies, it will be important in our future studies to validate

the role of mast cells in mediating antibiotic-induced perturbations of the microbiota in BrCa by performing studies in mast cell-deficient mice (Dudeck et al., 2011; Feyerabend et al., 2011; Grimbaldeston et al., 2005). Though in this regard, it is worth reiterating that mast cells have been shown to drive tumor growth and metastases in the MMTV-PyMT BrCa model in Kit$^{W-sh/W-sh}$ mice (He et al., 2016).

SUPPLEMENTAL INFORMATION

Supplemental information can be found online at https://doi.org/10.1016/j.isci.2021.103012.

STAR★ METHODS

Detailed methods are provided in the online version of this paper and include the following:

- KEY RESOURCES TABLE
- RESOURCE AVAILABILITY
  - Lead contact
  - Material availability
  - Data and code availability
- EXPERIMENTAL MODELS AND SUBJECT DETAILS
  - Animals
  - Animal experimentation
  - VNMAA and cephalexin antibiotic administration
  - Commensal administration
  - Cromolyn administration
  - Breast cancer cell culture
  - PyMT-BO1, BRPKp110 and EO771 tumor growth assays
  - Spontaneous breast cancer model (for mast cell counts)
  - ER+ Luminal A breast cancer model (for mast cell counts)
  - Passive FMT
- METHOD DETAILS
  - Cryo-sectioning of snap frozen tumors
  - Tissue processing (for H&E and IHC staining)
  - H&E staining
  - Toluidine blue staining
  - Picro-Sirius Red staining
  - Immunohistochemistry
  - Flow cytometry
  - Caecal DNA extraction
  - Shotgun metagenomics
  - Caecal Metabolomics
  - Mesoscale discovery multiplex arrays
  - Whole tumor RNA sequencing
  - Single cell RNA sequencing
- QUANTIFICATION AND STATISTICAL ANALYSIS

ACKNOWLEDGMENTS

AUTHOR CONTRIBUTIONS

Conceptualization, T.K., L.J.H., and S.D.R.; formal analyses, A.M.M., B.M.K., M.M., W.J.F., C.A.P., S.A.D., R.A., K.A.M., S.C., G.L.G., J.P., C.L., M.D., C.A.-G., A.A., T.-Y.F., M.D.M., T.T., M.R.R., L.J.H., and S.D.R.; investigation, A.M.M., B.M.K., M.M., W.J.F., C.A.P., R.A., K.A.M., S.C., G.L.G., J.P., C.L., M.D., C.A.-G., A.A., T.-Y.F., M.D.M., T.T., E.T., S.W.F.M., K.N.W., M.R.R., T.K., L.J.H., and S.D.R.; resources, S.W.F.M., K.N.W., M.R.R., T.K., L.J.H., and S.D.R.; review and editing, A.M.M., W.J.F., C.A.P., S.A.D., K.A.M., S.C., G.L.G., J.P., C.L., M.D., C.A.-G., A.A., T.-Y.F., M.D.M., T.T., E.T., S.W.F.M., K.N.W., M.R.R., T.K., L.J.H., and S.D.R.; visualization, A.M.M., B.K.M., M.M., W.J.F., C.A.P., R.A., G.L.G., T.-Y.F., T.K., L.J.H., and S.D.R.; supervision, E.T., S.W.F.M., K.N.W., M.R.R., T.K., L.J.H., and S.D.R.; funding acquisition, L.J.H. and S.D.R.

DECLARATION OF INTERESTS

INCLUSION AND DIVERSITY

REFERENCES

Allegrezza, M.J., Rutkowski, M.R., Stephen, T.L., Svoronos, N., Perales-Puchalt, A., Nguyen, J.M., Payne, K.K., Singhal, S., Eruslanov, E.B., Tchou, J., and Conejo-Garcia, J.R. (2016). Trametinib drives T-cell-dependent control of KRAS-mutated tumors by inhibiting pathological myelopoiesis. Cancer Res. 76, 6253–6265. https://doi.org/10.1158/0008-5472.CAN-16-1308.

Aminov, R.I. (2010). A brief history of the antibiotic era: lessons learned and challenges for the future. Front Microbiol. 1, 134. https://doi.org/10.3389/fmicb.2010.00134.

Andrews, S. (2010). FastQC: a quality control tool for high throughput sequence data, [Online]. Available online at: http://www.bioinformatics.babraham.ac.uk/projects/fastqc/.

Aponte-Lopez, A., Fuentes-Panana, E.M., Cortes-Munoz, D., and Munoz-Cruz, S. (2018). Mast cell, the neglected member of the tumor microenvironment: role in breast cancer. J. Immunol. Res. 2018, 2584243. https://doi.org/10.1155/2018/2584243.

Appleyard, C.B., Cruz, M.L., Isidro, A.A., Arthur, J.C., Jobin, C., and De Simone, C. (2011). Pretreatment with the probiotic VSL#3 delays transition from inflammation to dysplasia in a rat model of colitis-associated cancer. Am. J. Physiol. Gastrointest. Liver Physiol. 301, G1004–G1013. https://doi.org/10.1152/ajpgi.00167.2011.

Becattini, S., Taur, Y., and Pamer, E.G. (2016). Antibiotic-induced changes in the intestinal microbiota and disease. Trends Mol. Med. 22, 458–478. https://doi.org/10.1016/j.molmed.2016.04.003.

Becht, E., McInnes, L., Healy, J., Dutertre, C.A., Kwok, I.W.H., Ng, L.G., Ginhoux, F., and Newell, E.W. (2018). Dimensionality reduction for visualizing single-cell data using UMAP. Nat. Biotechnol. 37, 38–44. https://doi.org/10.1038/nbt.4314.

Beghini, F., McIver, L.J., Blanco-Miguez, A., Dubois, L., Asnicar, F., Maharjan, S., Mailyan, A., Thomas, A.M., Manghi, P., Valles-Colomer, M., Scholz, M., Weingart, G., Zhang, Y., Zolfo, M., Huttenhower, C., Segata, N., et al. (2021). Integrating taxonomic, functional, and strain-level profiling of diverse microbial communities with bioBakery 3. eLife 10, e65088. https://doi.org/10.7554/eLife.65088.

Benito, A., Polat, I.H., Noe, V., Ciudad, C.J., Marin, S., and Cascante, M. (2017). Glucose-6-phosphate dehydrogenase and transketolase modulate breast cancer cell metabolic reprogramming and correlate with poor patient outcome. Oncotarget 8, 106693–106706. https://doi.org/10.18632/oncotarget.21601.

Boyd, N.F., Guo, H., Martin, L.J., Sun, L., Stone, J., Fishell, E., Jong, R.A., Hislop, G., Chiarelli, A., Minkin, S., and Yaffe, M.J. (2007). Mammographic density and the risk and detection of breast cancer. N. Engl. J. Med. 356, 227–236. https://doi.org/10.1056/NEJMoa062790.

Bray, F., Ferlay, J., Soerjomataram, I., Siegel, R.L., Torre, L.A., and Jemal, A. (2018). Global cancer statistics 2018: GLOBOCAN estimates of incidence and mortality worldwide for 36 cancers in 185 countries. CA Cancer J. Clin. 68, 394–424. https://doi.org/10.3322/caac.21492.

Bray, N.L., Pimentel, H., Melsted, P., and Pachter, L. (2016). Near-optimal probabilistic RNA-seq quantification. Nat. Biotechnol. 34, 525–527. https://doi.org/10.1038/nbt.3519.

Buchfink, B., Xie, C., and Huson, D.H. (2015). Fast and sensitive protein alignment using DIAMOND. Nat. Methods 12, 59–60. https://doi.org/10.1038/nmeth.3176.

Buchta Rosean, C., Bostic, R.R., Ferey, J.C.M., Feng, T.Y., Azar, F.N., Tung, K.S., Dozmorov, M.G., Smirnova, E., Bos, P.D., and Rutkowski, M.R. (2019). Preexisting commensal dysbiosis is a host-intrinsic regulator of tissue inflammation and tumor cell dissemination in hormone receptor-positive breast cancer. Cancer Res. 79, 3662–3675. https://doi.org/10.1158/0008-5472.CAN-18-3464.

Bush, K., and Bradford, P.A. (2016). β-Lactams and β-lactamase inhibitors: an overview. Cold Spring Harb. Perspect. Med. 6, a025247. https://doi.org/10.1101/cshperspect.a025247.

Carmi, Y., Spitzer, M.H., Linde, I.L., Burt, B.M., Prestwood, T.R., Perlman, N., Davidson, M.G., Kenkel, J.A., Segal, E., Pusapati, G.V., et al. (2015). Allogeneic IgG combined with dendritic cell

stimuli induce antitumour T-cell immunity. Nature *521*, 99–104. https://doi.org/10.1038/nature14424.

Castagnoli, L., Iezzi, M., Ghedini, G.C., Ciravolo, V., Marzano, G., Lamolinara, A., Zappasodi, R., Gasparini, P., Campiglio, M., Amici, A., et al. (2014). Activated d16HER2 homodimers and SRC kinase mediate optimal efficacy for trastuzumab. Cancer Res. *74*, 6248–6259. https://doi.org/10.1158/0008-5472.CAN-14-0983.

Chen, S., Zhou, Y., Chen, Y., and Gu, J. (2018). fastp: an ultra-fast all-in-one FASTQ preprocessor. Bioinformatics *34*, i884–i890. https://doi.org/10.1093/bioinformatics/bty560.

Correa-Oliveira, R., Fachi, J.L., Vieira, A., Sato, F.T., and Vinolo, M.A. (2016). Regulation of immune cell function by short-chain fatty acids. Clin. Transl Immunol. *5*, e73. https://doi.org/10.1038/cti.2016.17.

Croswell, A., Amir, E., Teggatz, P., Barman, M., and Salzman, N.H. (2009). Prolonged impact of antibiotics on intestinal microbial ecology and susceptibility to enteric Salmonella infection. Infect. Immun. *77*, 2741–2753. https://doi.org/10.1128/IAI.00006-09.

De Zuani, M., Dal Secco, C., and Frossi, B. (2018). Mast cells at the crossroads of microbiota and IBD. Eur. J. Immunol. *48*, 1929–1937. https://doi.org/10.1002/eji.201847504.

DeNardo, D.G., Barreto, J.B., Andreu, P., Vasquez, L., Tawfik, D., Kolhatkar, N., and Coussens, L.M. (2009). CD4(+) T cells regulate pulmonary metastasis of mammary carcinomas by enhancing protumor properties of macrophages. Cancer Cell *16*, 91–102. https://doi.org/10.1016/j.ccr.2009.06.018.

DiLillo, D.J., Yanaba, K., and Tedder, T.F. (2010). B cells are required for optimal CD4+ and CD8+ T cell tumor immunity: therapeutic B cell depletion enhances B16 melanoma growth in mice. J. Immunol. *184*, 4006–4016. https://doi.org/10.4049/jimmunol.0903009.

Dudeck, A., Dudeck, J., Scholten, J., Petzold, A., Surianarayanan, S., Kohler, A., Peschke, K., Vohringer, D., Waskow, C., Krieg, T., et al. (2011). Mast cells are key promoters of contact allergy that mediate the adjuvant effects of haptens. Immunity *34*, 973–984. https://doi.org/10.1016/j.immuni.2011.03.028.

Edwards, B.L., Stukenborg, G.J., Brenin, D.R., and Schroen, A.T. (2014). Use of prophylactic postoperative antibiotics during surgical drain presence following mastectomy. Ann. Surg. Oncol. *21*, 3249–3255. https://doi.org/10.1245/s10434-014-3960-7.

Ewens, A., Mihich, E., and Ehrke, M.J. (2005). Distant metastasis from subcutaneously grown E0771 medullary breast adenocarcinoma. Anticancer Res. *25*, 3905–3915.

Feyerabend, T.B., Weiser, A., Tietz, A., Stassen, M., Harris, N., Kopf, M., Radermacher, P., Moller, P., Benoist, C., Mathis, D., et al. (2011). Cre-mediated cell ablation contests mast cell contribution in models of antibody- and T cell-mediated autoimmunity. Immunity *35*, 832–844. https://doi.org/10.1016/j.immuni.2011.09.015.

Franzosa, E.A., McIver, L.J., Rahnavard, G., Thompson, L.R., Schirmer, M., Weingart, G., Lipson, K.S., Knight, R., Caporaso, J.G., Segata, N., and Huttenhower, C. (2018). Species-level functional profiling of metagenomes and metatranscriptomes. Nat. Methods *15*, 962–968. https://doi.org/10.1038/s41592-018-0176-y.

Goedert, J.J., Jones, G., Hua, X., Xu, X., Yu, G., Flores, R., Falk, R.T., Gail, M.H., Shi, J., Ravel, J., and Feigelson, H.S. (2015). Investigation of the association between the fecal microbiota and breast cancer in postmenopausal women: a population-based case-control pilot study. J. Natl. Cancer Inst. *107*, djv147. https://doi.org/10.1093/jnci/djv147.

Gopalakrishnan, V., Spencer, C.N., Nezi, L., Reuben, A., Andrews, M.C., Karpinets, T.V., Prieto, P.A., Vicente, D., Hoffman, K., Wei, S.C., et al. (2018). Gut microbiome modulates response to anti-PD-1 immunotherapy in melanoma patients. Science *359*, 97–103. https://doi.org/10.1126/science.aan4236.

Grimbaldeston, M.A., Chen, C.C., Piliponsky, A.M., Tsai, M., Tam, S.Y., and Galli, S.J. (2005). Mast cell-deficient W-sash c-kit mutant Kit W-sh/W-sh mice as a model for investigating mast cell biology in vivo. Am. J. Pathol. *167*, 835–848. https://doi.org/10.1016/S0002-9440(10)62055-X.

Guan, X., Ma, F., Sun, X., Li, C., Li, L., Liang, F., Li, S., Yi, Z., Liu, B., and Xu, B. (2020). Gut microbiota profiling in patients with HER2-negative metastatic breast cancer receiving metronomic chemotherapy of capecitabine compared to those under conventional dosage. Front. Oncol. *10*, 902. https://doi.org/10.3389/fonc.2020.00902.

Han, X., Wang, R., Zhou, Y., Fei, L., Sun, H., Lai, S., Saadatpour, A., Zhou, Z., Chen, H., Ye, F., et al. (2018). Mapping the mouse cell atlas by microwell-seq. Cell *172*, 1091–1107.e1017. https://doi.org/10.1016/j.cell.2018.02.001.

Hannon. (2010). FASTX-Toolkit [Online], Available online at: http://hannonlab.cshl.edu/fastx_toolkit/contact.html.

He, C., Liu, Y., Ye, S., Yin, S., and Gu, J. (2021). Changes of intestinal microflora of breast cancer in premenopausal women. Eur. J. Clin. Microbiol. Infect. Dis. *40*, 503–513. https://doi.org/10.1007/s10096-020-04036-x.

He, L., Zhu, Z., Chen, S., Wang, Y., and Gu, H. (2016). Mammary tumor growth and metastasis are reduced in c-Kit mutant Sash mice. Cancer Med. *5*, 1292–1297. https://doi.org/10.1002/cam4.696.

Hothorn, T., Hornik, K., van de Wiel, M.A.V., and Zeileis, A. (2008). Implementing a class of permutation tests: the coin package. J. Stat. Softw. *28*, 1–23.

Hughes, E.R., Winter, M.G., Duerkop, B.A., Spiga, L., Furtado de Carvalho, T., Zhu, W., Gillis, C.C., Buttner, L., Smoot, M.P., Behrendt, C.L., et al. (2017). Microbial respiration and formate oxidation as metabolic signatures of inflammation-associated dysbiosis. Cell Host Microbe *21*, 208–219. https://doi.org/10.1016/j.chom.2017.01.005.

Huo, C.W., Hill, P., Chew, G., Neeson, P.J., Halse, H., Williams, E.D., Henderson, M.A., Thompson, E.W., and Britt, K.L. (2018). High mammographic

density in women is associated with protumor inflammation. Breast Cancer Res. *20*, 92. https://doi.org/10.1186/s13058-018-1010-2.

Jones, D.J., Bunn, F., and Bell-Syer, S.V. (2014). Prophylactic antibiotics to prevent surgical site infection after breast cancer surgery. Cochrane Database Syst. Rev. *9*, CD005360. https://doi.org/10.1002/14651858.CD005360.pub4.

Kelly, D., and Mulder, I.E. (2012). Microbiome and immunological interactions. Nutr. Rev. *70*, S18–S30. https://doi.org/10.1111/j.1753-4887.2012.00498.x.

Kim, D., Pertea, G., Trapnell, C., Pimentel, H., Kelley, R., and Salzberg, S.L. (2013). TopHat2: accurate alignment of transcriptomes in the presence of insertions, deletions and gene fusions. Genome Biol. *14*, R36. https://doi.org/10.1186/gb-2013-14-4-r36.

Lakritz, J.R., Poutahidis, T., Levkovich, T., Varian, B.J., Ibrahim, Y.M., Chatzigiagkos, A., Mirabal, S., Alm, E.J., and Erdman, S.E. (2014). Beneficial bacteria stimulate host immune cells to counteract dietary and genetic predisposition to mammary cancer in mice. Int. J. Cancer *135*, 529–540. https://doi.org/10.1002/ijc.28702.

Lechowski, S., Feilhauer, K., Staib, L., Coeffier, M., Bischoff, S.C., and Lorentz, A. (2013). Combined arginine and glutamine decrease release of de novo synthesized leukotrienes and expression of proinflammatory cytokines in activated human intestinal mast cells. Eur. J. Nutr. *52*, 505–512. https://doi.org/10.1007/s00394-012-0353-1.

Love, M.I., Huber, W., and Anders, S. (2014). Moderated estimation of fold change and dispersion for RNA-seq data with DESeq2. Genome Biol. *15*, 550. https://doi.org/10.1186/s13059-014-0550-8.

Marchini, C., Gabrielli, F., Iezzi, M., Zenobi, S., Montani, M., Pietrella, L., Kalogris, C., Rossini, A., Ciravolo, V., Castagnoli, L., et al. (2011). The human splice variant Delta16HER2 induces rapid tumor onset in a reporter transgenic mouse. PLoS One *6*, e18727. https://doi.org/10.1371/journal.pone.0018727.

Matson, V., Fessler, J., Bao, R., Chongsuwat, T., Zha, Y., Alegre, M.L., Luke, J.J., and Gajewski, T.F. (2018). The commensal microbiome is associated with anti-PD-1 efficacy in metastatic melanoma patients. Science *359*, 104–108. https://doi.org/10.1126/science.aao3290.

Mazurek, N., Berger, G., and Pecht, I. (1980). A binding site on mast cells and basophils for the anti-allergic drug cromolyn. Nature *286*, 722–723. https://doi.org/10.1038/286722a0.

McCafferty, J., Muhlbauer, M., Gharaibeh, R.Z., Arthur, J.C., Perez-Chanona, E., Sha, W., Jobin, C., and Fodor, A.A. (2013). Stochastic changes over time and not founder effects drive cage effects in microbial community assembly in a mouse model. ISME J. *7*, 2116–2125. https://doi.org/10.1038/ismej.2013.106.

McCoy, T.H., Castro, V.M., Snapper, L.A., Hart, K.L., and Perlis, R.H. (2017). Efficient genome-wide association in biobanks using topic modeling identifies multiple novel disease loci. Mol. Med. *23*, 285–294. https://doi.org/10.2119/molmed.2017.00100.

Metzger-Filho, O., Sun, Z., Viale, G., Price, K.N., Crivellari, D., Snyder, R.D., Gelber, R.D., Castiglione-Gertsch, M., Coates, A.S., Goldhirsch, A., and Cardoso, F. (2013). Patterns of Recurrence and outcome according to breast cancer subtypes in lymph node-negative disease: results from international breast cancer study group trials VIII and IX. J. Clin. Oncol. *31*, 3083–3090. https://doi.org/10.1200/JCO.2012.46.1574.

Minutello, K., and Gupta, V. (2021). Cromolyn Sodium (StatPearls).

Mullard, A. (2016). Tackling antimicrobial drug resistance. Nat. Rev. Drug Discov. *15*, 375. https://doi.org/10.1038/nrd.2016.115.

Naeini, M.B., Momtazi, A.A., Jaafari, M.R., Johnston, T.P., Barreto, G., Banach, M., and Sahebkar, A. (2019). Antitumor effects of curcumin: a lipid perspective. J. Cell Physiol *234*, 14743–14758. https://doi.org/10.1002/jcp.28262.

Oka, T., Kalesnikoff, J., Starkl, P., Tsai, M., and Galli, S.J. (2012). Evidence questioning cromolyn's effectiveness and selectivity as a 'mast cell stabilizer' in mice. Lab. Invest. *92*, 1472–1482. https://doi.org/10.1038/labinvest.2012.116.

Parhi, L., Alon-Maimon, T., Sol, A., Nejman, D., Shhadeh, A., Fainsod-Levi, T., Yajuk, O., Isaacson, B., Abed, J., Maalouf, N., et al. (2020). Breast cancer colonization by *Fusobacterium nucleatum* accelerates tumor growth and metastatic progression. Nat. Commun. *11*, 3259. https://doi.org/10.1038/s41467-020-16967-2.

Perez-Solis, M.A., Maya-Nunez, G., Casas-Gonzalez, P., Olivares, A., and Aguilar-Rojas, A. (2016). Effects of the lifestyle habits in breast cancer transcriptional regulation. Cancer Cell Int *16*, 7. https://doi.org/10.1186/s12935-016-0284-7.

Qian, B.Z., and Pollard, J.W. (2010). Macrophage diversity enhances tumor progression and metastasis. Cell *141*, 39–51. https://doi.org/10.1016/j.cell.2010.03.014.

R Core Team (2013). R: A language and environment for statistical computing, version 3.6.2 (Vienna, Austria: R Foundation for Statistical Computing). http://www.R-project.org/.

Ranganathan, K., Sears, E.D., Zhong, L., Chung, T.T., Chung, K.C., Kozlow, J.H., Momoh, A.O., and Waljee, J.F. (2018). Antibiotic prophylaxis after immediate breast reconstruction: the reality of its efficacy. Plast. Reconstr. Surg. *141*, 865–877. https://doi.org/10.1097/PRS.0000000000004204.

Rao, V.P., Poutahidis, T., Ge, Z., Nambiar, P.R., Boussahmain, C., Wang, Y.Y., Horwitz, B.H., Fox, J.G., and Erdman, S.E. (2006). Innate immune inflammatory response against enteric bacteria *Helicobacter hepaticus* induces mammary adenocarcinoma in mice. Cancer Res. *66*, 7395–7400. https://doi.org/10.1158/0008-5472.CAN-06-0558.

Rasouli, B.S., Ghadimi-Darsajini, A., Nekouian, R., and Iragian, G.R. (2017). In vitro activity of probiotic *Lactobacillus reuteri* against gastric cancer progression by downregulation of urokinase plasminogen activator/urokinase plasminogen activator receptor gene expression. J. Cancer Res. Ther. *13*, 246–251. https://doi.org/10.4103/0973-1482.204897.

Reikvam, D.H., Erofeev, A., Sandvik, A., Grcic, V., Jahnsen, F.L., Gaustad, P., McCoy, K.D., Macpherson, A.J., Meza-Zepeda, L.A., and Johansen, F.E. (2011). Depletion of murine intestinal microbiota: effects on gut mucosa and epithelial gene expression. PLoS One *6*, e17996. https://doi.org/10.1371/journal.pone.0017996.

Rooks, M.G., and Garrett, W.S. (2016). Gut microbiota, metabolites and host immunity. Nat. Rev. Immunol. *16*, 341–352. https://doi.org/10.1038/nri.2016.42.

Rossini, A., Rumio, C., Sfondrini, L., Tagliabue, E., Morelli, D., Miceli, R., Mariani, L., Palazzo, M., Menard, S., and Balsari, A. (2006). Influence of antibiotic treatment on breast carcinoma development in proto-neu transgenic mice. Cancer Res. *66*, 6219–6224. https://doi.org/10.1158/0008-5472.CAN-05-4592.

Routy, B., Le Chatelier, E., Derosa, L., Duong, C.P.M., Alou, M.T., Daillere, R., Fluckiger, A., Messaoudene, M., Rauber, C., Roberti, M.P., et al. (2018). Gut microbiome influences efficacy of PD-1-based immunotherapy against epithelial tumors. Science *359*, 91–97. https://doi.org/10.1126/science.aan3706.

Schwarzer, M., Hermanova, P., Srutkova, D., Golias, J., Hudcovic, T., Zwicker, C., Sinkora, M., Akgun, J., Wiedermann, U., Tuckova, L., et al. (2019). Germ-free mice exhibit mast cells with impaired functionality and gut homing and do not develop food allergy. Front. Immunol. *10*, 205. https://doi.org/10.3389/fimmu.2019.00205.

Segata, N., Waldron, L., Ballarini, A., Narasimhan, V., Jousson, O., and Huttenhower, C. (2012). Metagenomic microbial community profiling using unique clade-specific marker genes. Nat. Methods *9*, 811–814. https://doi.org/10.1038/nmeth.2066.

Sivan, A., Corrales, L., Hubert, N., Williams, J.B., Aquino-Michaels, K., Earley, Z.M., Benyamin, F.W., Lei, Y.M., Jabri, B., Alegre, M.L., et al. (2015). Commensal Bifidobacterium promotes antitumor immunity and facilitates anti-PD-L1 efficacy. Science *350*, 1084–1089. https://doi.org/10.1126/science.aac4255.

Stuart, T., Butler, A., Hoffman, P., Hafemeister, C., Papalexi, E., Mauck, W.M., 3rd, Hao, Y., Stoeckius, M., Smibert, P., and Satija, R. (2019). Comprehensive integration of single-cell data. Cell *177*, 1888–1902.e21. https://doi.org/10.1016/j.cell.2019.05.031.

Su, X., Esser, A.K., Amend, S.R., Xiang, J., Xu, Y., Ross, M.H., Fox, G.C., Kobayashi, T., Steri, V., Roomp, K., et al. (2016). Antagonizing integrin beta3 increases immunosuppression in cancer. Cancer Res. *76*, 3484–3495. https://doi.org/10.1158/0008-5472.CAN-15-2663.

Sung, H., Ferlay, J., Siegel, R.L., Laversanne, M., Soerjomataram, I., Jemal, A., and Bray, F. (2021). Global cancer statistics 2020: GLOBOCAN estimates of incidence and mortality worldwide for 36 cancers in 185 countries. CA Cancer J. Clin. *71*, 209–249. https://doi.org/10.3322/caac.21660.

Tabula Muris, C.; Overall coordination; Logistical coordination; Organ collection and processing; Library preparation and sequencing; Computational data analysis; Cell type annotation; Writing group; Supplemental text writing group; Principal investigators (2018).

Single-cell transcriptomics of 20 mouse organs creates a Tabula Muris. Nature *562*, 367–372. https://doi.org/10.1038/s41586-018-0590-4.

Tanoue, T., Morita, S., Plichta, D.R., Skelly, A.N., Suda, W., Sugiura, Y., Narushima, S., Vlamakis, H., Motoo, I., Sugita, K., et al. (2019). A defined commensal consortium elicits CD8 T cells and anti-cancer immunity. Nature *565*, 600–605. https://doi.org/10.1038/s41586-019-0878-z.

Tao, H., Lu, L., Xia, Y., Dai, F., Wang, Y., Bao, Y., Lundy, S.K., Ito, F., Pan, Q., Zhang, X., et al. (2015). Antitumor effector B cells directly kill tumor cells via the Fas/FasL pathway and are regulated by IL-10. Eur. J. Immunol. *45*, 999–1009. https://doi.org/10.1002/eji.201444625.

Teng, N.M.Y., Price, C.A., McKee, A.M., Hall, L.J., and Robinson, S.D. (2021). Exploring the impact of gut microbiota and diet on breast cancer risk and progression. Int. J. Cancer *149*, 494–504. https://doi.org/10.1002/ijc.33496.

Tomayko, M.M., and Reynolds, C.P. (1989). Determination of subcutaneous tumor size in athymic (nude) mice. Cancer Chemother. Pharmacol. *24*, 148–154. https://doi.org/10.1007/BF00300234.

Trapnell, C., Hendrickson, D.G., Sauvageau, M., Goff, L., Rinn, J.L., and Pachter, L. (2013). Differential analysis of gene regulation at transcript resolution with RNA-seq. Nat. Biotechnol. *31*, 46–53. https://doi.org/10.1038/nbt.2450.

Tremaroli, V., and Backhed, F. (2012). Functional interactions between the gut microbiota and host metabolism. Nature *489*, 242–249. https://doi.org/10.1038/nature11552.

University of California Los Angeles. Department of Statistics., and Foundation for Open Access Statistics. Journal of statistical software. Foundation for Open Access Statistics. UCLA Statistics

Varricchi, G., Galdiero, M.R., Loffredo, S., Marone, G., Iannone, R., Marone, G., and Granata, F. (2017). Are mast cells MASTers in cancer? Front Immunol. *8*, 424. https://doi.org/10.3389/fimmu.2017.00424.

Velicer, C.M., Heckbert, S.R., Lampe, J.W., Potter, J.D., Robertson, C.A., and Taplin, S.H. (2004). Antibiotic use in relation to the risk of breast cancer. JAMA *291*, 827–835. https://doi.org/10.1001/jama.291.7.827.

Velicer, C.M., Heckbert, S.R., Rutter, C., Lampe, J.W., and Malone, K. (2006). Association between antibiotic use prior to breast cancer diagnosis and breast tumour characteristics (United States). Cancer Causes Control *17*, 307–313. https://doi.org/10.1007/s10552-005-0445-9.

Vetizou, M., Pitt, J.M., Daillere, R., Lepage, P., Waldschmitt, N., Flament, C., Rusakiewicz, S., Routy, B., Roberti, M.P., Duong, C.P., et al. (2015). Anticancer immunotherapy by CTLA-4 blockade relies on the gut microbiota. Science *350*, 1079–1084. https://doi.org/10.1126/science.aad1329.

Viaud, S., Saccheri, F., Mignot, G., Yamazaki, T., Daillere, R., Hannani, D., Enot, D.P., Pfirschke, C., Engblom, C., Pittet, M.J., et al. (2013). The intestinal microbiota modulates the anticancer immune effects of cyclophosphamide. Science

342, 971–976. https://doi.org/10.1126/science.1240537.

Wagner, J., Rapsomaniki, M.A., Chevrier, S., Anzeneder, T., Langwieder, C., Dykgers, A., Rees, M., Ramaswamy, A., Muenst, S., Soysal, S.D., et al. (2019). A single-cell atlas of the tumor and immune ecosystem of human breast cancer. Cell *177*, 1330–1345.e1318. https://doi.org/10.1016/j.cell.2019.03.005.

Wang, C.C., Wu, H., Lin, F.H., Gong, R., Xie, F., Peng, Y., Feng, J., and Hu, C.H. (2018). Sodium butyrate enhances intestinal integrity, inhibits mast cell activation, inflammatory mediator production and JNK signaling pathway in weaned pigs. Innate Immun. *24*, 40–46. https://doi.org/10.1177/1753425917741970.

Wickham, H. (2016). ggplot2: Elegant Graphics for Data Analysis, 2nd Edition (Springer International Publishing). https://doi.org/10.1007/978-3-319-24277-4.

Wood, D.E., Lu, J., and Langmead, B. (2019). Improved metagenomic analysis with Kraken 2. Genome Biol. *20*, 257. https://doi.org/10.1186/s13059-019-1891-0.

Wu, A.H., Tseng, C., Vigen, C., Yu, Y., Cozen, W., Garcia, A.A., and Spicer, D. (2020). Gut microbiome associations with breast cancer risk factors and tumor characteristics: a pilot study. Breast Cancer Res. Treat *182*, 451–463. https://doi.org/10.1007/s10549-020-05702-6.

Wu, N., Yang, X., Zhang, R., Li, J., Xiao, X., Hu, Y., Chen, Y., Yang, F., Lu, N., Wang, Z., et al. (2013). Dysbiosis signature of fecal microbiota in colorectal cancer patients. Microb. Ecol. *66*, 462–470. https://doi.org/10.1007/s00248-013-0245-9.

Yuen, G.J., Demissie, E., and Pillai, S. (2016). B lymphocytes and cancer: a love-hate relationship. Trends Cancer *2*, 747–757. https://doi.org/10.1016/j.trecan.2016.10.010.

Zagato, E., Pozzi, C., Bertocchi, A., Schioppa, T., Saccheri, F., Guglietta, S., Fosso, B., Melocchi, L., Nizzoli, G., Troisi, J., et al. (2020). Endogenous murine microbiota member *Faecalibaculum rodentium* and its human homologue protect from intestinal tumour growth. Nat. Microbiol. *5*, 511–524. https://doi.org/10.1038/s41564-019-0649-5.

Zhang, T., Finn, D.F., Barlow, J.W., and Walsh, J.J. (2016). Mast cell stabilisers. Eur. J. Pharmacol.

778, 158–168. https://doi.org/10.1016/j.ejphar.2015.05.071.

Zhang, Z.G., Zhang, H.S., Sun, H.L., Liu, H.Y., Liu, M.Y., and Zhou, Z. (2019). KDM5B promotes breast cancer cell proliferation and migration via AMPK-mediated lipid metabolism reprogramming. Exp. Cell Res *379*, 182–190. https://doi.org/10.1016/j.yexcr.2019.04.006.

Zhu, J., Liao, M., Yao, Z., Liang, W., Li, Q., Liu, J., Yang, H., Ji, Y., Wei, W., Tan, A., et al. (2018). Breast cancer in postmenopausal women is associated with an altered gut metagenome. Microbiome *6*, 136. https://doi.org/10.1186/s40168-018-0515-3.

Zitvogel, L., Galluzzi, L., Viaud, S., Vetizou, M., Daillere, R., Merad, M., and Kroemer, G. (2015). Cancer and the gut microbiota: an unexpected link. Sci. Transl Med. *7*, 271ps271. https://doi.org/10.1126/scitranslmed.3010473.

Zitvogel, L., Pietrocola, F., and Kroemer, G. (2017). Nutrition, inflammation and cancer. Nat. Immunol. *18*, 843–850. https://doi.org/10.1038/ni.3754.

STAR★ METHODS

KEY RESOURCES TABLE

REAGENT or RESOURCE	SOURCE	IDENTIFIER
Antibodies		
CD45_PerCP-Cy5.5 (clone 30-F11)	eBioscience	CAT #: 45-0451; RRID: AB_1107002, AB_10324454
CD3_APC (clone 145-2C11)	eBioscience	CAT #: 17-0031; RRID: AB_469315
CD4_PE (clone GK1.5)	eBioscience	CAT #: 12-0041; RRID: AB_465506
CD8_PE-Cy7 (clone 53-6.7)	eBioscience	CAT #: 561967; RRID: AB_10893346
FoxP3 _eFluor450 (clone FJK-165)	eBioscience	CAT #: 48-5773; RRID: AB_1518813
CD19_BV650 (clone 6D5)	BioLegend	CAT #: 115541; RRID: AB_11204087
CD11b_AlexaFluor 700 (clone M1/70)	eBioscience	CAT #: 56-0112-80; RRID: AB_657585
F4/80_PE-Cy5 (clone BM8)	eBioscience	CAT #: 15-4801; RRID: AB_468797
Ly6G_APC-Cy7 (clone IA8)	BD	CAT #: 560600; RRID: B_1727561
CD206_PE (clone C068C2)	BioLegend	CAT #: 141705; RRID: AB_10896421
MHCII_eFluor450 (clone M5/114.1.2)	eBioscience	CAT #: 48-5321-82; RRID: AB_1272204
Anti-Ki67	Abcam	CAT #: ab15580; RRID: AB_443209
Anti-Endomucin (clone V.7C7)	Santa Cruz	CAT #: sc-65495; RRID: AB_2100037
Polyclonal Goat anti-Rabbit immunoglobulins/HRP	Agilent	CAT #: P0448, RRID:AB_2617138'
Polyclonal Rabbit anti-Rat immunoglobulins/HRP	Agilent	CAT #: P0450, RRID:AB_2630354
Bacterial and virus strains		
Faecalibaculum rodentium (Type strain 103405)	DSMZ	DSM 103405
Chemicals, peptides, and recombinant proteins		
Amphotericin-B	Merck Life Science	CAT #: A2411
Ampicillin	Merck Life Science	CAT #: A9518
Vancomycin Hydrochloride	Fisher Scientific	CAT #: 11956911
Metronidazole	Merck Life Science	CAT #: M3761
Neomycin trisulfate salt hydrate	Merck Life Science	CAT #: N1876
Cephalexin	Merck Life Science	CAT #: C4895
Cromolyn Sodium	Merck Life Science	CAT#: C0399
Toluidine Blue-O	Merck	CAT #: 198161
Safranin-O	Abcam	CAT #: ab146329
Alcian Blue 8GX	Merck Life Science	CAT #: A3157
Harris Hematoxylin Soultion	Merck Life Science	CAT#: HHS128
Eosin	Merck Life Science	CAT#: HT110116
Critical commercial assays		
MPBio FastDNA SPIN Kit for Soil	MPBio	CAT #: 116560200
Mesoscale Discovery V-PLEX Pro-inflammatory Panel 1 Mouse Kit	MSD	CAT #: K15048D
Foxp3/Transcription Factor Staining Buffer Kit	eBioscience	CAT #: 00-5523-00
Fetal bovine serum	Gibco	CAT #: 10500-064
Dulbecco's Modified Eagle's Medium - High Glucose	Merck Life Science	CAT #: D6429
Pen Strep	Gibco	CAT #: 15140-122
70µm Cell Strainer	Corning Costar	CAT#: 352350
Live/Dead_Green	Thermofisher	CAT #: L34970

Continued

REAGENT or RESOURCE	SOURCE	IDENTIFIER
Live/Dead_Red	Thermofisher	CAT #: L34971
Collagenase type IV	Gibco	CAT #: 17104-019
Hyaluronidase from sheep testes	Merck Life Science	CAT #: H6254
Deoxyribonuclease 1 from bovine pancreas	Merck Life Science	CAT #: D4263
Deposited data		
Shotgun metagenomics files	This manuscript	ENA : PRJEB40951
Bulk RNA-seq files	This manuscript	ENA : PRJEB40951
scRNA-seq files	This manuscript	ENA : PRJEB40951
Experimental models: Cell lines		
PyMT-BO1 cells	From Katherine Weilbaecher	(Su et al., 2016)
EO771 cells	Kind gift from Jeffrey Pollard	(Ewens et al., 2005)
BRPKp110 cells	From Melanie Rutkowski	(Buchta Rosean et al., 2019)
Experimental models: Organisms/strains		
Wild-type C57 mice	Bred in-house at UEA Disease Modeling Unit	Originally from Charles River, C57BL/6NCrl
Delta16HER2 transgenic FVB mice	(Marchini et al., 2011)	N/A
Software and algorithms		
GraphPad Prism 9	GraphPad Software	9.1.0
FlowJo	FlowJo	V10
Omics Explorer	Qlucore	3.6
BBDuk	sourceforge.net/projects/bbmap/	v.38.76
BBMap	sourceforge.net/projects/bbmap/	v38.76
MetaPhlAn v3.0	(Segata et al., 2012)	R package
ggplot2	Wickham, 2016	R package
FastQC	(Andrews, 2010)	0.11.3
FASTX-Toolkit	(Hannon, 2010)	0.1.5
Tophat	(Kim et al., 2013)	2.1.1
Cufflinks	(Trapnell et al., 2013)	2.1.0
Kallisto	(Bray et al., 2016)	R package
DeSeq2	(Love et al., 2014)	R Package
Cell ranger v2.0	10X Genomics	2.0.0
Seurat V3.0	Stuart et al. 2019	R package
HUMAnN3	(Franzosa et al., 2018)	v3.0.0.alpha
Kraken2	Wood et al., 2019	v2.1.0
Fastp	Chen et al., 2018	v0.21.0
DIAMOND	Buchfink et al., 2015	v0.9.24
R	R Core Team 2013	v3.6.2
Coin	(Hothorn et al., 2008)	v1.4-1; R package
Stats	R	v3.6.2; R package
BioRender	https://biorender.com/	Under individual license to lead contact, Stephen Robinson
Other		
Axio Imager M2	Zeiss	N/A
LSRFortessa flowcytometer	BD	N/A

RESOURCE AVAILABILITY

Lead contact

Requests for further information, resources and reagents should be directed to and will be fulfilled by the lead contact, Dr. Stephen Robinson, Gut Microbes and Health Program, Quadram Institute Bioscience, Norwich Research Park, Norwich, UK, Stephen.Robinson@uea.ac.uk.

Material availability

This study has not generated new unique reagents.

Data and code availability

Shotgun metagenomic, Bulk RNA-seq and scRNA-seq data have been deposited at European Nucleotide Archive (ENA) and are publicly available as of the date of publication. Accession numbers are listed in the key resources table.

No original code was used in the analysis of data presented in this manuscript. All packages and pro-grammes used for data analysis are listed in the key resources table.

EXPERIMENTAL MODELS AND SUBJECT DETAILS

Animals

All animals for orthotopic studies were female C57BL/6 mice and were sourced in-house. All animals were age matched at 8–10 weeks old. All animal experiments were performed in accordance with UK Home Office regulations and the European Legal Framework for the Protection of Animals used for Scientific Purposes (European Directive 86/609/EEC).

Animal experimentation

To minimize experimental bias, mice were pooled and randomly allocated to treatment groups at the start of each experiment. Subsequently, animals from each treatment group (which generally required housing across multiple cages) were pooled and randomly re-distributed at each gavage/additional treatment. Wherever possible, experimental measurements (e.g. tumor volume measurements) were performed blind.

VNMAA and cephalexin antibiotic administration

Animals were treated with antibiotics three times weekly by oral gavage (200μL in water). Animals were treated with either a cocktail consisting of 0.2 mg/ml Amphoteracin B (Merck Life Science, Gillingham, UK), 5 mg/ml Vancomycin (Merck Life Science), 10 mg/ml Neomycin (Merck Life Science), 10 mg/ml Metronidazole (Merck Life Science) with drinking water being supplemented with 1 mg/ml Ampicillin (Merck Life Science) or 43.2 mg/ml Cephalexin (Merck Life Science). Antibiotic treatment began 5 days prior to orthotopic cell injection and was maintained throughout animal experiments.

Commensal administration

Faecalibaculum rodentium (DSMZ, Type strain 103405) was cultured in Peptone Yeast Glucose (PYG) broth and harvested at optical density (OD) 0.6, via centrifugation (2770 rcf, 10 min, 4°C). Pellets were washed twice in Phosphate Buffered Saline (PBS) before final resuspension in PBS. Bacteria were administered three times per week by oral gavage (250 μL).

Cromolyn administration

Animals were treated with VNMAA antibioitcs three times weekly and orthotopically induced with a PyMT-BO1 BrCa as described previously. From 10 days post tumor induction, animals received a daily intraperitoneal injection of cromolyn sodium (Merck Life Science) (10 mg/kg, 100 μL) alongside continued oral antibioitcs until experimental cessation 15 days after tumor induction.

Breast cancer cell culture

Cells were cultured in high glucose DMEM (Thermofisher, Carlsbad, California, US) supplemented with 10% fetal bovine serum (FBS) (Hyclone, Thermofisher) and 100 units/mL penicillin/streptomycin (Pen/Strep)

(Thermofisher). Cells were maintained at 37°C and 5% CO_2. Tissue culture plastic was coated with 0.1% porcine gelatin (Merck Life Science) in water for 1 hr at 37°C prior to culture.

PyMT-BO1, BRPKp110 and EO771 tumor growth assays

PyMT-BO1 or EO771 (1×10^5) cells or BRPKp110 (5×10^5) cells were injected at 50µL per animal at a 1:1 mixture of PBS and Matrigel (Corning Life Sciences, Corning, New York, USA) into the left abdominal mammary fat pad (MFP) of age matched female mice. At experimental endpoint, animals were sacrificed by cervical dislocation and tissues harvested for various downstream analyses. Tumors were measured in two dimensions (Length x Width) using digital calipers. Tumor volume was calculated according to the following formula: (length $\times$ width^2 $\times$ 0.52 (Tomayko and Reynolds, 1989).

Spontaneous breast cancer model (for mast cell counts)

Delta16HER2 transgenic FVB mice (Castagnoli et al., 2014; Marchini et al., 2011) were treated with Vancomycin (200 mg/L) in drinking water starting when mice were 4 weeks of age and continued to 6 weeks post tumor onset.

ER+ Luminal A breast cancer model (for mast cell counts)

Mice were orally gavaged (100 µL) for 14 days with antibiotic cocktail (0.5 mg/mL Vancomycin, 1 mg/mL Ampicillin, 1 mg/mL Metronidazole, 1 mg/mL Neomycin, and 1 mg/mL Gentamicin) or water. After 14 days of treatment, mice were left untreated for four days before initiation of mammary tumors, at which point 5×10^5 BRPKp110 cells were injected orthotopically into the abdominal mammary fat pad, as previously described (Buchta Rosean et al., 2019).

Passive FMT

Animals were not directly co-housed due to delivery of Ampicillin via drinking water, but co-housing was simulated by transfer of bedding and fecal pellets between cages. The antibiotic treatment regimen was followed as before, beginning five days prior to orthotopic cell injection, during which time animals from each experimental condition were housed separately. At tumor injection, water and VNMAA treated animals were provided bedding swaps. This was maintained throughout the experiment with bedding swaps every other day and antibiotic treatments were also continued throughout the experiment.

METHOD DETAILS

Cryo-sectioning of snap frozen tumors

Tumors were harvested from humanely killed animals, immediately placed in microcentrifuge tubes, snap frozen in liquid nitrogen and stored at −80°C. Tumors were subsequently sectioned at a thickness of 5µm on a Cryostat NX70 (Thermofisher) and sections were stored at −80°C until staining.

Tissue processing (for H&E and IHC staining)

Tissues were fixed overnight in 4% paraformaldehyde (PFA) and paraffin-embedded before being cut in 6 µm sections. Sections were deparaffinised and rehydrated in xylene followed by graded alcohol solutions to PBS prior to any subsequent staining.

H&E staining

Using a Leica ST5020 multistainer (Leica Biosystems, Milton Kenes, UK), sections were placed in Harris Hematoxylin (Merck Life Science) for five minutes followed by acid alcohol (70% ethanol, 1% hydrochloric acid) for 15 s, 0.1% sodium carbonate for 1 min and eosin (Merck Life Science-Adrich) for 30 s. Sections were then subject to a graded alcohol dehydration to xylene prior to mounting in an anhydrous mounting medium.

Toluidine blue staining

Frozen sections were air dried for 10 min at room temperature (RT) then fixed in ice-cold methanol for 10 min. Post-fixation, sections underwent three 2 min washes in distilled water before being placed in working toluidine blue solution for 3 min (working solution:Toluidine Blue O (Merck) was prepared in 70% ethanol and then added to 1% NaCl, pH 2.5 in a ratio of 1:10). Following staining, sections underwent three 2 min washes in distilled water followed by a gradual dehydration through 95% and 100% ethanol before being cleared in xylene and mounted using an anhydrous mounting medium.

Picro-Sirius Red staining

Frozen sections were air dried for 10 min at RT then fixed in 4% PFA for 10 min. Sections were covered with Picro-Sirius Red solution (Abcam, Cambridge, UK) and incubated for 60 min at RT. Sections were then washed twice in a 0.5% solution of acetic acid, dehydrated in three changes of 100% ethanol and cleared in xylene before being mounted mounting in an anhydrous mounting medium. Fibrosis was quantified using Image J software by calculating the area of tissue and the intensity of red staining.

Immunohistochemistry

Paraffin-embedded sections were blocked for endogenous peroxidases (3% H_2O_2 in methanol) prior to a citrate buffered antigen retrieval and blocking in a Tris-buffered saline (TBS), 10% goat serum, 0.1% Triton-X100 solution. Staining was performed using either polyclonal rabbit anti-Ki67 antibody (Abcam) or monoclonal rat anti-endomucin (Santa Cruz Biotechnology, Heidelberg, Germany) both at 1:1000 overnight at 4°C. Following a one-hour incubation with either a HRP conjugated anti-rabbit or anti-rat immunoglobulins (Agilent, Santa Clara, CA, USA) sections were developed with 3,3'-Diaminobenzidine (DAB) chromogen and quenched in water. Harris Hematoxylin (Merck Life Science) was used to counterstain prior to a graded alcohol dehydration and mounting in an anhydrous mounting medium. Quantification of the number of Ki67-positive cells was performed by an average count of two frames per tumor section expressed as a percentage of total cells per frame.

Flow cytometry

Organs were excised from humanely killed animals and tissues were mechanically homogenized using scalpels. Homogenate was incubated in collagenase solution (0.2% Collagenase IV (Thermofisher), 0.01% Hyaluronidase (Merck Life Science) & 2.5 U/ml DNAse I (Merck Life Science) in Hank's Balanced Salt Solution (HBSS) for 1 hr at 37°C with regular agitation. Supernatant was passed through a 70 μm cell strainer and centrifuged for 5 min at 300 x g/4°C. The pellet was washed twice in PBS and resuspended in 10 mL 1X red blood cell lysis buffer (Thermofisher) and incubated for 5 min at RT. Cells were washed once in PBS, counted using a hemocytometer and 1 million cells per condition transferred to a 96 well plate for staining. Cells were incubated in a fixable Live/Dead stain (Thermofisher) for 30 min at RT, washed twice and blocked in Fc Block (Miltenyi, Bergisch Gladbach, Germany) made in FACS buffer (1% FBS in PBS) for 10 min at 4°C. Cells were resuspended in 100μL antibody solutions and incubated at 4°C for 30 min in the dark. For cell surface only staining, cells were incubated in 4% PFA for 30 min, washed once in PBS and stored at 4°C until analyzed. If intracellular staining was required, cells were incubated in FoxP3 fixation/permeabilisation buffer (Thermofisher) overnight at 4°C, washed twice in 1X permeabilisation buffer (Thermofisher), blocked in 5% normal rat serum for 30 min at RT and stained in the relevant antibody diluted in 1X permeabilisation buffer for 30 min at RT in the dark. Cells were washed twice in 1X permeabilisation buffer, then finally resuspended in FACS buffer and stored at 4°C until analyzed.

All data was collected using a Becton Dickinson (BD, Franklin Lakes, NJ, USA) LSR Fortessa with standard filter sets and five lasers. Data was analyzed using FlowJo software (BD).

For all samples, single cells were gated via FSC-A against FSC-H followed by live cell selection as a Live/Dead® negative population and leukocytes through CD45+ staining. Pan-myeloid cells were gated as CD11b+ and subsequent populations including monocytic (Ly6C+), neutrophilic (Ly6G+) and macrophages (F4/80+) were identified from them. Macrophage activation was defined as 'M1' (MHCII+) or 'M2' (CD206+) from the F4/80+ population. Lymphocytes (CD3e+) were gated from a CD45+ population and divided into CD8+ and CD4+ populations with the CD4 population being further classified into T-regulatory cells though Foxp3+ staining. B-Cells (CD19+) were also gated directly from CD45+ populations. Gating strategies are detailed in Figure S3A.

Caecal DNA extraction

Caecal material or feces was weighed into MPBio Lysing Matrix E bead beating tubes (MPBio, Santa Ana, CA, USA) and extraction was completed according to the manufacturer's protocol for the MPBio FastDNA™ SPIN Kit for Soil but extending the beat beating time to 3 min. The DNA recovered from these samples was assessed using a Qubit® 2.0 fluorometer (Thermofisher).

Shotgun metagenomics

A modified Illumina Nextera low input tagmentation approach was used. 9 μL of TD Tagment DNA Buffer was mixed with 0.09 μL TDE1, Tagment DNA Enzyme and 4.01 μL PCR grade water in a master mix and 3 μL added to a chilled 96 well plate. Genomic DNA was normalized to 0.5ng/μL with 10 mM Tris-HCl. 2 μL of normalized DNA (1ng total) was pipette mixed with the 5 μL of the tagmentation mix and heated to 55 °C for 10 min in a PCR block.

A PCR master mix was made up using 4 ul kapa2G buffer, 0.4 μL dNTP's, 0.08 μL Polymerase and 4.52 μL PCR grade water, contained in the Kap2G Robust PCR kit (Merck Life Science) per sample and 9 μL added to each well need to be used in a 96-well plate. 2 μL of each P7 and P5 of Nextera XT Index Kit v2 index primers (Illumina) were added to each well. Finally, the 7 μL of Tagmentation mix was added and mixed. The PCR was run with 72°C for 3 min, 95°C for 1 min, 14 cycles of 95°C for 10s, 55°C for 20s and 72°C for 3 min.

Following the PCR reaction, the libraries were quantified using the Quant-iT dsDNA Assay Kit, high sensitivity kit and run on a FLUOstar Optima plate reader. Libraries were pooled following quantification in equal quantities. The final pool was double-SPRI size selected between 0.5 and 0.7X bead volumes using KAPA Pure Beads (Roche, Burgess Hill, UK). The final pool was quantified on a Qubit 3.0 instrument and run on a D5000 ScreenTape (Agilent) using the Agilent Tapestation 4200 to calculate the final library pool molarity.

The pool was run at a final concentration of 1.5 pM on an Illumina Nextseq500 instrument using a Mid Output Flowcell (NSQ® 500 Mid Output KT v2(300 CYS) following the Illumina recommended denaturation and loading recommendations which included a 1% PhiX spike in (PhiX Control v3 Illumina Catalog FC-110-3001). Data was uploaded to Basespace (www.basespace.illumina.com) where the raw data was converted to 8 FASTQ files for each sample.

Human and mouse contamination was removed from raw reads by using Kraken2 v2.1.0 (1) with a confidence setting of 0.5 and minimum base quality 22 using the human genome GRCh38.p12 and mouse genome GRCm39 as reference databases. Decontaminated reads were trimmed to a quality of phred 20 and adapters removed using fastp v0.21.0 (2) and PhiX Illumina standards were removed with BBDuk v38.76 (sourceforge.net/projects/bbmap/). Clean reads from single samples were concatenated. Taxonomic profiling was performed on the filtered reads using MetaPhlAn v3.0 using the settings –unknown_estimation and –add_viruses and the Chocophlan database v30 (3). Functional profiling was performed with HUMAnN2 v3.0.0.alpha with search mode uniref90 and an uniref90 translated search database and using DIAMOND v0.9.24 (4). The results were normalized to relative abundances.

Relative abundances of taxa and pathways were analyzed in R (R Core Team 2013) and visualized using the ggplot2 package (5). To test whether relative abundances of *F. rodentium* were significantly different in treatments VNMAA and Cephalexin compared to controls, we performed the Wilcoxon-Mann-Whitney test using the *wilcox_test* function in the *coin* package v1.4-1 (6). p values were adjusted for multiple testing using the Benjamini-Hochberg correction within the function *p.adjust* of the *stats* package v3.6.2. To determine bacterial species that were differentially abundant in the Cephalexin treatment compared to controls we pre-filtered the species table to remove taxa that were not detected one of the two experiments; not found in more than 5 samples; and those that had a coefficient of variation below 1. On the remaining 22 species we performed Wilcoxon-Mann-Whitney tests using the *wilcox_test* function in the *coin* package and adjusted the p value for multiple testing using the Benjamini-Hochberg correction within the function *p.adjust* of the *stats* package. Functional pathways were filtered and their relative abundances analyzed identically to species abundances (Beghini et al., 2021; Buchfink et al., 2015; Chen et al., 2018; University of California Los Angeles. Department of Statistics. and Foundation for Open Access Statistics.; Wickham, 2016; Wood et al., 2019). To visualize the magnitude and direction of change of functional pathways between treatments, sample difference between medians and their confidence intervals were extracted from the Wilcoxon-Mann-Whitney test results using the confint() from the coin package. These values were plotted and colored according to adjusted p values using the ggplot2 package. The deviation from an estimate of zero indicates direction of change with pathways enriched in cephalexin treatments to the right and pathways enriched in controls to the left side (Figure S6).

Caecal Metabolomics

Caecal contents (50–100 mg) were thoroughly mixed with 600–1200 μL NMR buffer made up of 0.1 M phosphate buffer (0.51 g Na2HPO4, 2.82 g K2HPO4, 100 mg sodium azide and 34.5 mg sodium 3-(Trimethylsilyl)-propionate-d4 (1 mM) in 200 mL deuterium oxide), centrifuged at 12,000 x g for 5 min at 4°C and supernatant transferred to 5-mm NMR tubes. ^{1}H NMR spectra were recorded on a 600MHz Bruker Avance spectrometer fitted with a 5 mm TCI cryoprobe (Bruker, Rheinstetten, Germany). Sample temperature was controlled at 300 K. Each spectrum consisted of 64 scans of 65,536 complex data points with a spectral width of 12.5 ppm (acquisition time 2.67 s). The noesypr1d presaturation sequence was used to suppress the residual water signal with low power selective irradiation at the water frequency during the recycle delay (D1 = 3 s) and mixing time (D8 = 0.01 s). A 90° pulse length of 9.6 μs was set for all samples. Spectra were manually phased, and baseline corrected using the TOPSPIN 2.0 software. Metabolites were identified and quantified using Chenomx ® software NMR suite 7.0^{TM}.

Statistical analysis and heatmapping of metabolite concentrations was performed using Qlucore Omics Explorer 3.6 software.

Mesoscale discovery multiplex arrays

Tissue samples were weighed into a MPBio Lysing Matrix E bead beating tube (MPBio) with 1 mL of homogenization buffer (PBS +10% fetal bovine serum (FBS) (Thermofisher) + cOmplete™ protease inhibitor (Roche). Tissues were homogenized using an MPBio Fast Prep bead beater at speed 4.0 for 40 s followed by speed 6.0 for 40 s. Samples were centrifuged at 12,000 x g for 12 min at 4°C and subsequently stored at −80°C until analyzed. Samples were run on a Mesoscale Discovery (MSD, Rockville, MD, USA) V-PLEX Pro-Inflammatory Panel 1 Mouse Kit according to the manufacturer's instructions. Plate was read using an MSD QuickPlex SQ 120 imager.

Whole tumor RNA sequencing

Frozen tissue was defrosted at 4°C and briefly homogenized using a scalpel. The homogenate was transferred to an MPBio Lysing Matrix E bead beating tube containing RNAbee (AMSBio, Cambridge, MA, USA) and homogenized using a TissueLyser LT. Extraction of RNA was performed using a phenol/choloroform method followed by purification of RNA using the SV Total RNA Isolation System (Promega) according to manufacturer's instructions. RNA concentration and purity was analyzed on a Nanodrop 2000 system (Thermofisher) to assess A260/280 and A260/230 ratios. Extracted RNA was then quality checked and quantified using a 2100 Bioanalyzer (Agilent) with an RNA 6000 Nano analysis kit (Agilent) and any samples with a RIN value of >8 were considered for use in sequencing. Suitable samples were sent to the Wellcome Trust Sanger Institute for sequencing. All samples were processed by poly-A selection and then sequenced using non-stranded, paired end protocol. Initial processing was performed at Welcome Trust Sanger Institute as follows. Data demultiplexed and adapter removed. Raw reads quality controlled using FastQC (0.11.3) and trimmed (phred score > 30) using FASTX (0.1.5). This was followed by read alignment to mouse reference genome (NCBI Mus musculus GRCm38) using Tophat (2.1.1) using maximum intron size 500.000 bp and default settings. Aligned transcripts were assembled and quantified using Cufflinks (2.1.0) (applying standard parameters).

Read alignment and quantification was performed using Kallisto. The quantified read data was then normalized and differential expression analysis was conducted using DeSeq2. Transcript IDs were annotated using the Ensembl Biomart database. Significantly up and downregulated genes (p_{adj} < 0.05) were used to perform biological process and pathway analysis using DAVID. Biological processes were annotated according to the GO_TERM_BP_ALL database and pathway analysis was performed using KEGG pathways. Significantly enriched pathways were determined by an enrichment score of less than 0.05, however scores of less than 0.1 were also evaluated as non-significantly altered pathways and processes.

Single cell RNA sequencing

Organs were excised from humanely killed animals and tissues were mechanically homogenized using scalpels. Homogenate was incubated in collagenase solution (0.2% Collagenase IV (Thermofisher), 0.01% Hyaluronidase (Merck Life Science) & 2.5 U/ml DNAse I (Merck Life Science) in HBSS) for 1 hr at 37°C with regular agitation. Supernatant was passed through a 70 μm cell strainer and centrifuged for 5 min at 300 x g/4°C. Pellet was washed twice in PBS and resuspended in 10mL 1X red blood cell lysis buffer

(Thermofisher) and incubated for 5 min at RT. Cells were washed once in PBS and resuspended in 10mL of 1% FBS in PBS before being handed to the Earlham Institute sequencing facility where they were run on the 10X Genomics™ Chromium platform.

BCL files were processed using bcl2fastq to create FASTQ files which were demultiplexed using Cell Ranger v2.0 aligned to the mm10 (GRCm38) mouse transcriptome and their = cell and unique molecular identifier (UMI) barcodes extracted. The resulting digital gene expression DGE matrices were processed using the R package Seurat V3.0 (Stuart et al., 2019). As a quality control step, the DGE matrices were filtered to remove low-quality cells (genes detected in less than five cells and cells where < 200 genes had non-zero counts) and library size normalization to obtain the normalized counts.

Datasets were integrated in Seurat v3.0 (Stuart et al., 2019) using a non-linear transformation of the underlying data and identified anchors from FindIntegrationAnchors used to integrate across the datasets. The top 2500 highly variable genes were selected and the integrated dataset was scaled. Initial clustering was performed using a Louvain algorithm with default parameters within Seurat's FindClusters function (Stuart et al., 2019) and a single PCA applied to both datasets to project onto two dimensions with UMAP clustering.

Differential expression analysis was performed using combined data from the four datasets. Genes were identified as differentially expressed in each cluster by comparing the gene expression of cells in the cluster with that of all the other cells. The top differentially expressed genes for each cluster were identified as cluster marker genes and ranked by their adjusted p values and average log-fold change. The top cluster marker genes were compared to cell type marker genes identified in the literature and used for cell-type identification (Han et al., 2018; Tabula Muris et al., 2018; Wagner et al., 2019).

QUANTIFICATION AND STATISTICAL ANALYSIS

Unless otherwise noted, data as normally distributed and *p* values were generated using Student's *t* test (GraphPad Prism, version 9.1) (unpaired, two-tailed, at 95% confidence interval) or One-way ANOVA where appropriate. *p* values are indicated directly in the figures; ns = not significant ($P > 0.05$).